

University of Nevada, Reno

**Predicting Micro-catchment Poned Infiltration
Dynamics**

**A thesis submitted in partial fulfillment of the requirements for the Degree of
Master of Science in Hydrology**

by

Michael Founds

Dr. Kenneth McGwire, Thesis Advisor

August 2018



We recommend that the thesis
prepared under our supervision by

MICHAEL FOUNDS

entitled

Predicting Micro-catchment Pondered Infiltration Dynamics

be accepted in partial fulfillment of the
requirements for the degree of

MASTER OF SCIENCE

Kenneth McGwire, Ph.D., Advisor

Mark Wertz, Ph.D., Committee Member

Paul Verberg, Ph.D., Graduate School Representative

David W. Zeh, Ph.D., Dean, Graduate School

August, 2018

Abstract

Rainfall and concentrated flow experiments were carried out on seven micro-catchments (MCs) that were designed to represent a rangeland restoration strategy using the Vallerani Plow. Prediction of infiltration rates within catchments is necessary to quantify potential benefits of restoration in a modeling framework. 3-D models of MC geometry and continuous stage measurements were used to calculate infiltration rates from field data. Soil samples and Guelph Permeameter (GP) measurements were collected to parameterize a predictive infiltration model. A 2-D simplified cross-section was developed to represent the MCs in Hydrus 2D/3D. The model domain was set up to mimic field simulations, and allowed for rainfall, evaporation, and time-varying ponded water levels. The antecedent rainfall and ponded water levels that were specific to each MC were applied in Hydrus models over a 400-minute simulation. Predicted velocity of water across the catchment boundary was averaged by depth intervals and multiplied against the surface area of that interval to calculate a volumetric flow rate. The soil at the field site had highly variable conductivity, both vertically within the soil profile and between sites. Consequently, four separate models of changes in conductivity with depth were evaluated, resulting in 28 total model runs. Model results were compared to measured infiltration data for six time intervals after the catchment was filled and began draining. The magnitude of predicted volumetric flow rates was highly variable and dependent on the K_s profile used. Use of the maximum field measured conductivity in the Hydrus model provided the best results, though it underpredicted measured flow rates by an average of 12%. Underprediction is likely due to preferential pathways that are not considered in the uniform flow model, the small size of GP measurements relative to the MC and use of a 2-D model to represent 3-D flow. Many opportunities exist to expand the modeling approach to test hypotheses on rangeland erosion and infiltration dynamics, and to develop optimal configurations of MCs at sites being considered for mitigation.

Contents

Abstract.....	i
Table of Contents.....	ii
List of Tables.....	iv
List of Figures.....	v
1 Introduction.....	1
2 Background.....	7
2.1 Physical Models of Infiltration.....	7
2.2 Soil Water Retention Curve.....	9
2.3 Guelph Permeameter.....	10
2.4 Analytical Solutions to Pondered Infiltration.....	13
2.5 Hydrus.....	15
2.5.1 Boundary Conditions.....	16
2.5.2 Rosetta.....	17
2.5.3 Nonequilibrium Flow Models.....	18
3 Methods.....	20
3.1 Site Description.....	20
3.2 Micro-catchment Design.....	21
3.3 Micro-catchment Instrumentation and Sampling.....	23
3.3.1 Micro-catchment Instrumentation.....	24
3.3.2 Soil Measurements and Sampling.....	25
3.3.3 Structure from Motion.....	27
3.3.4 Micro-catchment geometry.....	28
3.4 Rainfall Simulations.....	29
3.5 Concentrated Flow Simulation.....	30
3.6 Micro-catchment Infiltration Model.....	32

3.7	Hydrus Model	34
3.7.1	Hydrus Model Geometry	34
3.7.2	Boundary Conditions	37
3.7.3	Hydrus 2-D Model Development.....	39
3.7.4	Hydrus 2-D vs Axisymmetric Model Comparison	40
3.7.5	Conductivity Profiles	42
4	Results	43
4.1	Soils Analysis.....	43
4.2	Micro-catchment Stage to Surface Area and Volume.....	44
4.3	Concentrated Flow Infiltration.....	46
4.3.1	Hydrus Model Outputs.....	47
4.4	Velocity Profile Conversion to Volumetric Flow Rate.....	49
4.4.1	Velocity Profile.....	50
4.4.2	Volumetric Flow Rate Calculation	51
4.5	Modeled and Measured Results Comparison.....	51
4.6	2-D vs. Axisymmetric Results	57
5	Discussion	59
5.1	K_s Profile 1.....	59
5.2	K_s Profile 2.....	60
5.3	K_s Profile 3.....	61
5.4	K_s Profile 4.....	62
5.5	Improvements and Next Steps	63
6	Conclusion.....	65
7	Literature Cited.....	67
8	Appendices	70

List of Tables

Table 2.1 Key terminology to describe soil hydraulic models.	7
Table 3.1 Typical pedon description of Bedell Series [NRCS, 2017].....	21
Table 3.2 Values used for GP calculations.....	26
Table 3.3 Rainfall intensity, duration, and total rainfall applied to each MC.	30
Table 4.1 PSD data analysis and Rosetta Lite 1.1 neural network prediction of hydraulic parameters.....	43
Table 4.2 2017 GP K_{fs} results averaged from wells on each side of a MC (cm/min).	44
Table 4.3 2018 GP K_{fs} results averaged from wells on each side of a MC and within berm (cm/min).....	44
Table 4.4 Maximum GP K_{fs} values for upper, lower, and average of the two hillslope positions at each depth interval (cm/min).	44
Table 4.5 Velocity Profile for U4 (Full Results Displayed in Appendices).....	51
Table 4.6 Measured vs. modeled volumetric flow rates with K_s Profile 1	53
Table 4.7 Measured vs. modeled volumetric flow rate with K_s Profile 2.	54
Table 4.8 Measured vs. modeled volumetric flow rate with K_s Profile 3.	55
Table 4.9 Measured vs. modeled volumetric flow rate with K_s Profile 4	56
Table 4.10 Measured vs. Modeled average values comparison by site for all K_s Profiles.....	57

Table 4.11 Change in velocity and volumetric flow rate model results (original – axisymmetric).	58
--	----

List of Figures

Figure 1.1 Overview of Mancos Shale Formation within the Upper Colorado River Basin (UCRB)	2
Figure 2.1 On the left, the field saturated bulb represented by K_{fs} directly adjacent well, and the wetted but unsaturated zone represented by Φ_m . On the right, the size of the term ($K_{fs}/\Phi_m = \alpha^*$) can be seen for a variety of soils [reproduced from Elrick et al., 1989]	12
Figure 2.2 Figure from Siumnek and van Genuchten [2008] displaying flow models of increasing complexity that can be applied in Hydrus 1-D.	19
Figure 3.1 Overview of Bedell flat area with locations of MCs and percent slope.	20
Figure 3.2 MC morphology created from 3-D model sent from Jordan showing recently constructed MC by Vallerani Plow [Strohmeier, 2017].....	23
Figure 3.3 MC instrumentation with WGRS, box simulator, and SR.....	25
Figure 3.4 Schematic overview of soil particle size distribution (PSD) sampling and Guelph Permeameter (GP) measurements for lower MCs.	27
Figure 3.5 MC predictive infiltration model to yield velocity profile with soil depth.....	33
Figure 3.6 Simple representation of upper sites with soil layers.	35
Figure 3.7 Hydrus model geometry.	36
Figure 3.8 Finite element mesh refinements.	36

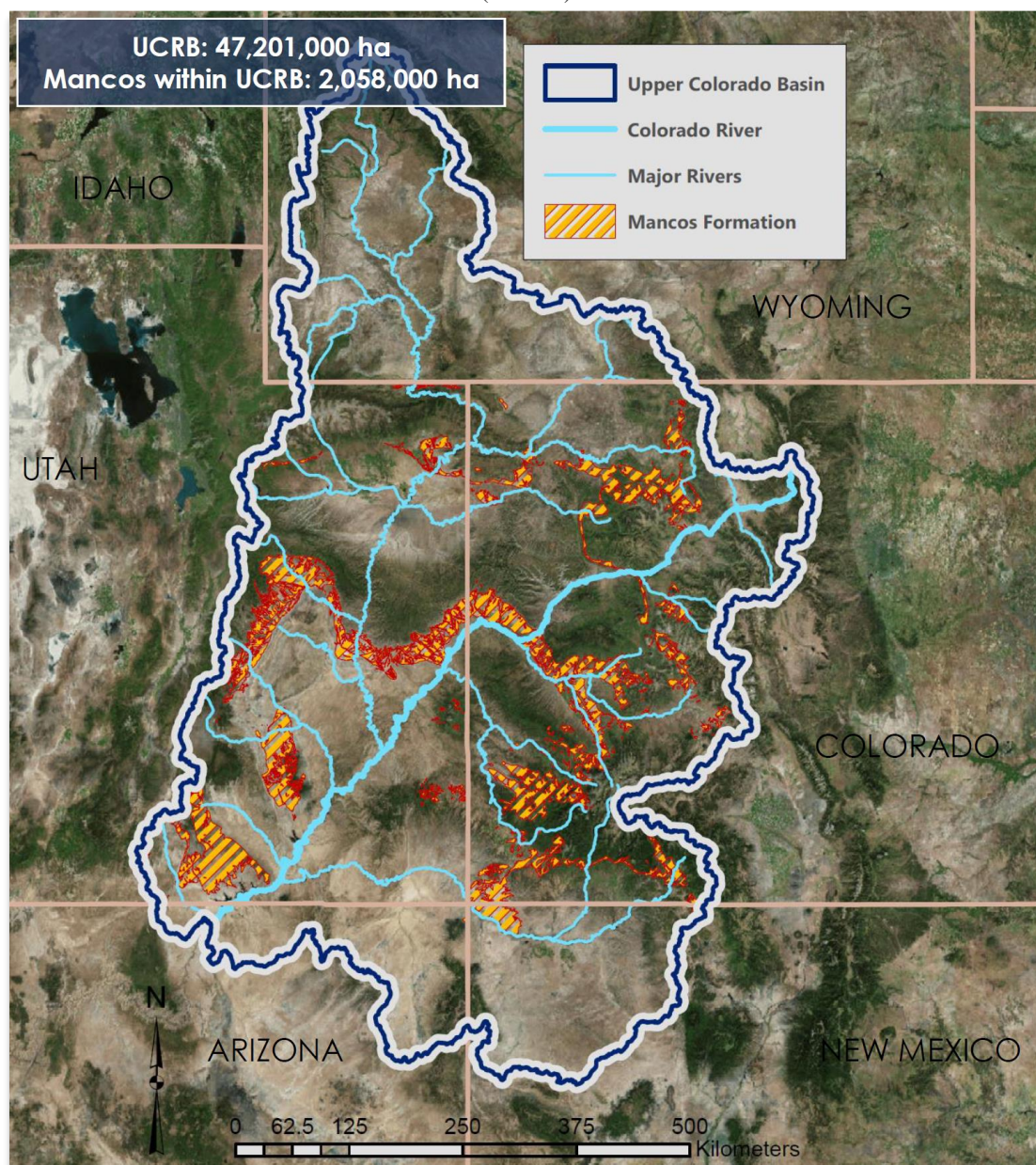
Figure 3.9 Hydrus model boundary conditions.....	38
Figure 3.10 Example of time varying boundary condition at 10 cm elevation within MC.....	39
Figure 3.11 Comparison of 2-D Vertical Plane and 2-D Axisymmetric model domains	40
Figure 3.12 Comparison of 2-D Vertical Plane and 2-D Axisymmetric model domains.	41
Figure 4.1 Relationship between stage in each MC to 3-D Surface Area.....	45
Figure 4.2 Relationship between stage in each MC to Volume.	45
Figure 4.3 Volumetric flow rate for the 60 minutes after water inflow was stopped.	46
Figure 4.4 Pressure Head distribution for L1 at 255 minutes.	47
Figure 4.5 Water Content distribution for L1 at 255 minutes.....	48
Figure 4.6 Velocity vectors for L1 at 255 minutes.	49
Figure 4.7 Velocity distribution for L1 at 255 minutes.	49

1 Introduction

This research is being performed in support of the goals of the Colorado River Basin Salinity Control Program, which seeks to address the threat of salinity to the 35–40 million people who depend on water within the Colorado River Basin. The Colorado River Basin Salinity Control Act of 1974 requires the Colorado River supply to meet water quality standards for total dissolved solids (TDS) for downstream uses, including international obligations to Mexico. The Salinity Control Program currently helps prevent 1.25 million tons of salt per year from entering the Colorado river, and strives to meet a goal of 1.85 million tons of salt per year by 2030 [*Bureau of Reclamation*, 2017]. A model developed by the Bureau of Reclamation estimated that economic damages of salinity levels in 2010 was 295 million dollars, primarily impacting agricultural (52%) and industrial (28%) sectors [*Bureau of Reclamation*, 2013]. Almost half (47%) of salinity within the Colorado river is estimated to come from natural sources such as erosion of saline geologic formations [*Bureau of Reclamation*, 2013]. These sources of erosion on federally managed rangeland within the Upper Colorado River Basin (UCRB) are being considered for mitigation. Over 47 million hectares of land within the UCRB are covered by the Mancos Shale formation, which is known to contribute disproportionately high levels of salinity to the Colorado River (Figure 1.1). One study evaluating rangelands in Utah found that while only 15% of area was in severely eroding condition, these areas contributed 75 – 90% of the total dissolved solids load [*Rasely et al.*, 1991]. These highly erodible lands represent an opportunity to reduce salinity through targeted restoration practices [*Weltz et al.*, 2008]. This research will evaluate how a restoration strategy using micro-catchments (MCs) with a characteristic geometry created by the Vallerani plow might promote infiltration on saline rangelands. The process of infiltrating excess runoff into MCs is expected to reduce erosion, but there is a lack of research exploring erosion and infiltration dynamics of restoration strategies. Results of this effort will

improve the ability of resource managers to make informed decisions regarding restoration practices on semi-arid saline rangelands of the Mancos Formation, which account for over two million hectares within the UCRB (Fig. 1.1).

Figure 1.1 Overview of Mancos Shale Formation within the Upper Colorado River Basin (UCRB)



Soil erosion was recognized as a problem in the United States as early as the 1920's, and by 1935 was considered a "national menace" in over half of the country [Weaver and Noll, 1935]. The susceptibility of any soil to erode is dependent on complex interactions between topography, soils, vegetation, land use, and climate. Water erosion from raindrop splash and transport by thin flow across the soils surface can be referred to as either interrill or sheet erosion. As water is concentrated into distinct flow paths, the kinetic energy of the water increases. The turbulence and kinetic energy of the water can detach soil particles causing rills to form [NRCS, 2003]. Detached particles are transported downslope with the sheer stress of surface flow and eventually deposited as the water's kinetic energy decreases [Breshears *et al.*, 2003]. The complex surface of undisturbed rangelands that is covered in rocks, plant litter, woody debris, and biological crusts can shield soils and interrupt concentrated flow and subsequent erosion [Weltz *et al.*, 2008]. Conversely, rangelands that have been disturbed do experience erosion because of increases in concentrated flow. For example, in the 3-year period following a fire, runoff from concentrated flow can increase to 20 times the rates from unburnt hillslopes [Pierson *et al.*, 2008].

One way to mitigate erosion is to increase infiltration rates, thereby reducing the volume of concentrated flow that can cause erosion. MCs have traditionally been used for water harvesting in arid areas where runoff is captured within pits and is available for plants [Malagnoux, 2008; Oweis, 2017]. Projects are being implemented that mechanize the process of MC development with the Vallerani Plow System. The MCs have the benefit of capturing the water, dissipating its kinetic energy, and giving it time to infiltrate. Restoration techniques with the Vallerani System have been applied to nearly 100,000 ha of degraded areas in Morocco, Niger, Senegal, Sudan, Tunisia, Chad and Egypt [Malagnoux, 2008]. The Badia Benchmark Study carried out in Jordan and Syria found that intermittent contours created by the Vallerani plow proved to be an economical way to establish vegetation and reduce soil erosion [Oweis *et al.*, 2011]. Despite

wide application of this restoration strategy, there are knowledge gaps in the quantity of erosion expected from large rainfall events, as well as the infiltration dynamics within each MC.

The Vallerani system was originally developed in 1988 to mechanize traditional rainwater harvesting techniques using half-moon shaped pits using special ploughs [Oweis et al. 2011]. The process of constructing MCs and planting is relatively simple. A tractor pulls a plow perpendicular to a hillslope so that runoff from upslope flows into a MC. The plow includes a ripper and a curved metal blade used to push soil up. A hydraulic system allows the blade to move up in down in a wave motion to a depth of 40-50 cm within the soil. The blade scoops out the soil for 3.5 - 5 m before the blade is lifted, pushing the soil downslope to form a semi-circular berm 20-30 cm high. The exact size of catchments and their placement on a hillslope will depend on rainfall intensity, slope, and soil properties. Following construction, appropriate native species are planted within each MC. Runoff naturally flows into the MC from upslope, where it is captured and infiltrates into the subsurface. The increased water within the soil profile can give plants a chance to establish and grow. Over the course of a few years, the MCs fill in with soil and seeds from upslope. The Vallerani System enables restoration of degraded systems at a large scale. Restoration efforts in Jordan and Syria found that 20 hectares per day of MCs could be constructed at a cost of 32 USD/ha [Oweis, 2017]. An analysis of the suitability of lands for water harvesting in Jordan identified many additional areas where restoration would likely be effective [Ziadat et al., 2012]. However, minimal research has been carried out to determine how restoration with the Vallerani System could be applied in other arid and semi-arid regions of the world. Rangelands within the UCRB are being considered for restoration with the Vallerani System, but more research is necessary to determine the potential benefits for erosion management before implementation at the hillslope scale. In the UCRB, a primary goal of rangeland restoration is to reduce salinity reaching the Colorado River, making it critical to understand MC infiltration and erosion dynamics during high intensity rainfall events.

An operational strategy to implement MCs at the hillslope scale should be based on rainfall patterns for the area, slope, soil properties, as well as the predicted infiltration capacity for MCs. Precipitation in the UCRB often comes in the form of convective air-mass thunderstorms. These events can be difficult to model at the small watershed scale without high resolution rainfall data [Goodrich *et al.*, 1995]. To avoid uncertainties related to natural rainfall events, rainfall simulators are frequently used in semi-arid rangelands study runoff and erosion while controlling water application and initial conditions [Paige *et al.*, 2004]. Rainfall simulations on common rangeland plant communities has demonstrated that many biotic and abiotic factors control infiltration rates, and best modeling results utilized equations specific to a rangeland community [Spaeth *et al.*, 1996]. The inherent complexity of rangeland hydrologic processes makes it challenging to predict how a restoration strategy will function. Just like any engineered structure, MCs need to be sized and spaced adequately for optimal function and cost effectiveness. This research utilizes a combination of rainfall simulations and modeling techniques to improve our ability to predict the hydrologic function of MCs on rangelands. This will help determine if the soil and precipitation conditions make MC construction a viable strategy for hillslope restoration. If a location is feasible, increased understanding of MC infiltration dynamics will help determine optimal density of MC construction on a hillslope.

While the Jordan Badia Benchmark Project showed potential as a strategy to reduce erosion, little work has been done that is easily translatable to the UCRB. Estimates of erosion are based on a limited series of naturally occurring rainfall events and required further investigation of impact of MC spacing on erosion rates [Oweis *et al.*, 2011]. This makes it useful to understand MC function in a modeling framework, where different environmental scenarios could be tested to determine appropriate MC size and spacing at any location. The Agricultural Research Service (ARS) has developed the Rangeland Hydrology and Erosion Model (RHEM) to predict runoff and erosion rates specifically for rangelands [Nearing *et al.*, 2011; Hernandez *et al.*, 2017]. Representing

MCs hydrologic properties within RHEM will require in-depth understanding of the complex infiltration processes occurring within a MC. This research will develop a model to predict the infiltration dynamics within MCs, parameterized by soil texture and measurements with a Guelph permeameter (GP). The hypothesis is that unsaturated zone models developed for the Hydrus 2D/3D software package, combined with geometric information on micro-catchment design, can be used to predict the volumetric flowrate of water into the vadose zone. This information will provide an adaptable, quantitative basis for land managers to evaluate the potential benefits of large scale implementation of MCs as a restoration strategy in the UCRB.

2 Background

To better understand the physics of a MC, it is necessary to comprehend how physical models of infiltration were developed. The following sub-sections provide a historical background to our evolving understanding of soil physics in the unsaturated zone, focusing on the specific concepts utilized in this investigation. The key terminology used in the remainder of the document is described in Table 2.1.

Table 2.1 Key terminology to describe soil hydraulic models.

Term	Description	Units
Q	Volumetric flow rate	[L ³ T ⁻¹]
q	Flux of water	[LT ⁻¹]
K _s	Saturated hydraulic conductivity	[LT ⁻¹]
h	Capillary pressure head or hydrostatic potential	[L]
θ	Water content (percentage)	[L ³ /L ³]
K(h)	Unsaturated hydraulic conductivity as a function of pressure head	[LT ⁻¹]
K(θ)	Unsaturated hydraulic conductivity as a function of water content	[LT ⁻¹]
Se(h)	Effective saturation (percentage)	[L ³ /L ³]

2.1 Physical Models of Infiltration

The foundation of how saturated flow moves through porous media was developed by Darcy [1856] while experimenting with sand filtration systems. The empirical description is commonly known as Darcy's Law:

$$\frac{Q}{A} = -K_s \frac{\Delta h}{L} \quad (1)$$

The volumetric flow rate (Q) [L³T⁻¹] of water flowing over a cross-sectional area (A) [L²], is equal to a proportionality constant known as saturated hydraulic conductivity (K_s), multiplied by the change in hydraulic head between two points (Δh) [L] of saturated porous media.

For unsaturated flow, where the soil water content (θ) is less than the saturated water content (θ_s), the unsaturated hydraulic conductivity $K(\psi)$ is related to a function of capillary pressure head (ψ). Note that ψ refers to areas of negative pressure observed in the variably saturated zone and can be alternatively expressed as negative potential ($-h$). A positive h value can be referred to as hydrostatic potential, while a negative h value could be called matric potential. Since h can represent saturated (positive h) and unsaturated (negative h) flow, it will be used for the remainder of this document. Buckingham [1907] developed a modification of Darcy's equation for unsaturated conditions (Darcy-Buckingham Equation):

$$q = -K(\theta) \frac{dh}{dz} = -K(h) \left(\frac{dh}{dz} + \frac{dz}{dz} \right) = -K(h) \left(\frac{dh}{dz} + 1 \right) \quad (2)$$

The term q [LT^{-1}] is the flux of water, $-K(\theta)$ is the unsaturated hydraulic conductivity as a function of water content, and $K(h)$ is the unsaturated conductivity as a function of capillary pressure head. Z is the vertical coordinate (positive upwards), therefore the term dz/dz reduces to 1 and represents gravitationally driven fluxes.

By combining the work of Darcy and Buckingham with the law of conservation of mass, Richards [1931] developed an equation to represent flow through variably saturated media. Conservation of mass can be simplified as a function of water content in 3-D as the following function:

$$\frac{d(\theta)}{dt} = -\frac{dq_x}{dx} - \frac{dq_y}{dy} - \frac{dq_z}{dz} - S \quad (3)$$

The change in water content over time is equal to the flux in each dimension and S represents any sources or sinks. Under homogeneous, isotropic conditions, vertical infiltration can be expressed by substituting the Darcy-Buckingham equation, yielding the Richards equation in 1D.

$$\frac{d(\theta)}{dt} = -\frac{d}{dz} \left(-K(h) \left(\frac{dh}{dz} + 1 \right) \right) - S \quad (4)$$

The $K(h)$ term is the unsaturated conductivity as a function of matric potential. The term $\frac{dh}{dz}$ represents capillarity and is a function of h . The “1” term is the simplification of $\frac{dz}{dz}$ representing gravitational flow. The Richards equation is a highly complex partial differential equation that models flow in the unsaturated zone. Both $K(h)$ and $\frac{dh}{dz}$ are functions of h , making the equation nonlinear. While some analytical infiltration equations have been developed to simplify Richards equation, practical applications of Richards equation often require numerical solutions [Radcliffe, 2010].

2.2 Soil Water Retention Curve

The relationship between θ and h known as the soil water retention curve (SWRC), is widely used to model soil physical properties. The shape of the SWRC can be used to predict soil water storage, but it is highly dependent on soil texture. One early model proposed by Gardner [1958] assumed that the change in water content over time is related to the capillary conductivity multiplied by a function of capillary potential (h). This yielded a steady-state equation to predict unsaturated conductivity $K(h)$, but neglected to accurately portray the importance of soil texture. Many scientists worked to predict unsaturated hydraulic conductivity as a function of the SWRC based on the assumption that $K(\theta)$ is related to the size of interconnected capillary tubes. The size of the pore radii in the soil matrix control important properties of the SWRC such as the air entry pressure, which is defined by the matric potential at which water can fill the largest soil pore radius. Mualem (1976) made the connection that the air entry pressure is related to the largest

pore radius and suggested a frequently used expression to predict $K(\theta)$ as a function of the effective saturation $Se(h)$:

$$Se(h) = \text{effective saturation: } \frac{\theta - \theta_r}{\theta_s - \theta_r} \quad (5)$$

where θ_s is saturated water content and θ_r is residual water content. Residual water is the water held in films around soil matrix that does not drain due to gravity. The van Genuchten model is frequently used in conjunction with the model of Mualem to predict unsaturated conductivity $K(h)$ in the vadose zone. The van Genuchten model uses three fitting parameters to define the SWRC curve [van Genuchten, 1980].

$$Se(h) = 1 / [(-\alpha|h|)^n]^m \quad (6)$$

The term α [L^{-1}] is related to the inverse of the entry pressure. The n term is related to the pore size distributions. The m term is another shape factor which is usually set as a fixed relationship ($m=1/n$). The shape of the curve for a given soil is defined by the soil hydraulic parameters and allows for prediction of $K(h)$ given a known pressure head or water content. The SWRC between θ and h still forms the foundation for predicting infiltration in the unsaturated zone. Software such as Hydrus, along with the work discussed in the next sections, often use a combination the models of Mualem and van Genuchten to predict water flow within the vadose zone.

2.3 Guelph Permeameter

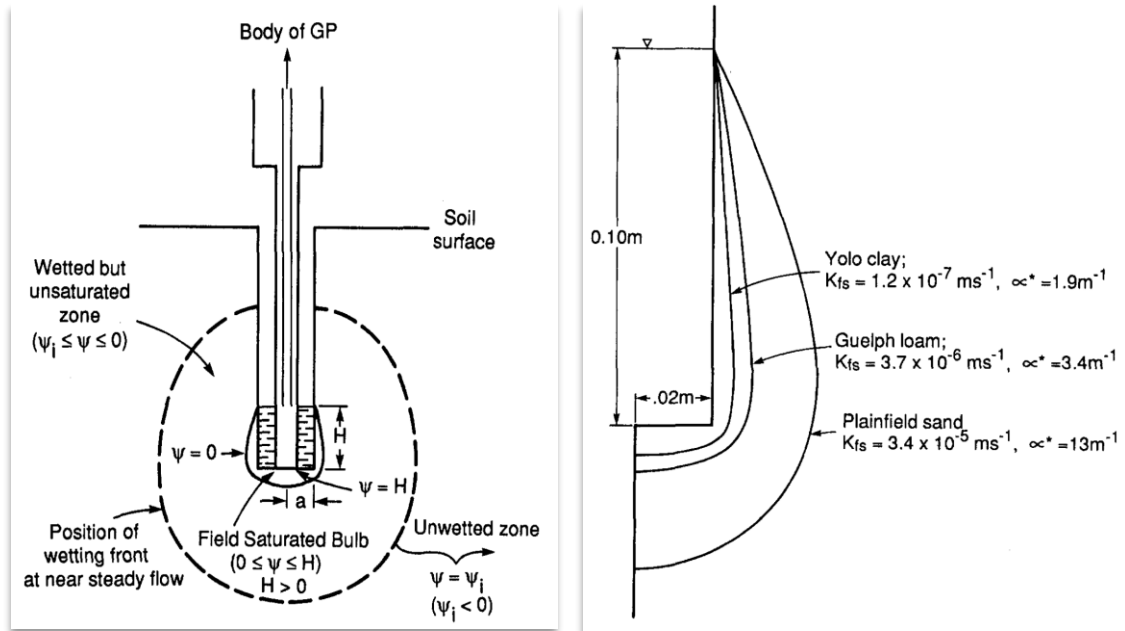
While many methods exist to measure physical soil properties in a laboratory environment, there are challenges in measuring these properties in the field. Soils can vary on a small spatial scale with location and depth. To understand infiltration dynamics in a MC, it is necessary to understand changes in conductivity with depth. The Guelph Permeameter (GP) utilizes the

Marriotte Principle to provide a field measure of steady state, in-situ flow rate for a range of depths in a borehole. A GP uses Richards and Laplace equations to obtain field-saturated hydraulic conductivity (K_{fs}) and matric flux potential (Φ_m) for flow out of a cylindrical well [Reynolds and Elrick, 1985]. Based on three-dimensional saturated-unsaturated flow theory, K_{fs} and Φ_m were determined to be the main soil hydraulic properties for determining field infiltration, rather than a percolation rate that does not account for capillarity [Reynolds and Elrick, 1986]. A simple conceptualization of steady flow from a cylindrical well is described as follows [Elrick *et al.*, 1989]:

$$Q = f(H, a)K_{fs} + G(H, a)\Phi_m \quad (7)$$

where H is the height of water ponded (cm), a is the radius of the well (cm), and f and g are functions of H . The first term in the equation models saturated flow within the soil. The field saturated conductivity (K_{fs}) is very similar to saturated conductivity (K_s), but is assumed to include air entrapped in soil which typically occurs during field infiltration. The GP also accounts for capillarity with the second term, the matric flux potential (Φ_m), which generally represents unsaturated flow. The GP functions by releasing water to a steady height within the cylindrical well. A small bulb of field saturated soil (K_{fs}) forms directly adjacent the well, and the zone between the saturated bulb and the wetting front is represented by the matric flux potential (Φ_m) term (Figure 2.1. Left). The size of and shape of the saturated bulb surrounding the well can be approximated by the ratio of field saturated conductivity to matric flux potential ($K_{fs}/\Phi_m = \alpha^*$) as seen on the right side of Figure 2.1. Values of α^* have been calculated for a range of soils with values varying from $\alpha^* = 1\text{m}^{-1}$ for compacted clays to 36m^{-1} for coarse sands and gravel [Elrick *et al.*, 1989].

Figure 2.1 On the left, the field saturated bulb represented by K_{fs} directly adjacent well, and the wetted but unsaturated zone represented by Φ_m . On the right, the size of the term ($K_{fs}/\Phi_m = \alpha^*$) can be seen for a variety of soils [reproduced from Elrick et al., 1989]



The expression for flow out of a cylindrical test hole is given below:

$$Q = AKfs + B\Phi m \quad (8)$$

$$A = (2\pi H^2/C + \pi a^2)$$

$$B = (2\pi H/C)$$

The A term reflects the well's bottom area and the cylindrical area of the well sides. B is only a function of capillarity and does not include the bottom area of the well. The term C is a dimensionless parameter that characterizes pressure head gradients across the saturated surface of the well [Reynolds and Elrick, 1986]. The C parameter is dependent on the height of well water (H), the radius (a), and soil texture; soil texture is not extremely significant allowing representation with three curves for sands, structured loams and clays, and unstructured clays as seen in equation 9 [Zhang et al., 1998]:

Shape Factor for structured loams and clays (C_2) [Zhang, 1998].

$$C_2 = \left[\frac{\frac{H}{a}}{1.992 + 0.091 \frac{H}{a}} \right]^{.683} \quad (9)$$

GP solutions can be obtained using a single ponded height or two ponded heights within the well. The two ponded head method has been noted to be more accurate for academic purposes, but vertical heterogeneity of the soil profile can cause erroneous results [Elrick *et al.*, 1989]. For the single ponded height method, K_{fs} and Φ_m can be calculated using the following equations:

$$K_{fs} = \frac{Q}{\left[A + \left(\frac{B}{\alpha^*} \right) \right]} = \frac{CQ}{\left[\left(\frac{2\pi H^2}{C} \right) + \pi a^2 C + \frac{2H}{\alpha^*} \right]} \quad (10)$$

$$\Phi_m = \frac{Q}{[A\alpha^* + B]} = \frac{CQ}{[2\pi H^2 + (\pi a^2 C)\alpha^* + 2\pi H]} \quad (11)$$

Use of a GP provides a simple test to measure K_{fs} and Φ_m at a range of depths. These variables help us comprehend infiltration processes that are happening in the more complex geometry of a MC.

2.4 Analytical Solutions to Ponded Infiltration

Numerous studies have developed approaches to create analytical solutions to the highly nonlinear Richards equation for specific infiltration scenarios. One approach, originally proposed by Gardner [1958], solves the Richards equation for steady state flow using an exponential model. Another common method uses moisture retention functions and unsaturated conductivity to solve for steady state infiltration [Broadbridge and White, 1988]. Neither of these models account for transient rainfall input for ponded infiltration. Solutions to 1-D transient infiltration have been proposed that use power law functions to solve for water content profiles [Hayek,

2014; 2016]. 2-D infiltration functions have been developed explicitly for furrows and provide a physically based mechanism to predict infiltration using a 1-D vertical infiltration and edge effects [Bautista *et al.*, 2016; Warrick *et al.*, 2007]. While these models are useful for certain applications, none of the models described above have a mechanism to deal with anisotropic soils.

Many other models have been developed to solve for infiltration by making assumptions about the depth of saturated water within the vadose zone. The Green-Ampt model provides a simple and frequently used implicit equation to estimate cumulative infiltration assuming a sharp wetting front between an upper saturated zone and lower unsaturated zone for a homogeneous isotropic soil with uniform moisture content [Green and Ampt, 1911]. One benefit of the Green-Ampt model is that it can be expressed to represent ponded infiltration assuming constant water content and capillary pressure [Selker *et al.*, 1999]. An explicit function to determine the depth of the wetting front of water infiltrating into soil can be used to refine Green-Ampt predictions, and accuracy of the model was found to be within 15% of numerical simulations using Richards equation [Selker and Assouline, 2017]. The simplicity of the Green-Ampt model has led to its widespread integration into hydrologic models. A comprehensive review of seven commonly used explicit Green-Ampt models [Ali *et al.*, 2016] ranked each by performance solving hydrologic problems. An expression developed by Bower for recharge from vadose zone wells estimates volumetric flow rate based on well hydraulic conductivity and water table depth [Bouwer, 2002], and was modified to predict infiltration rates in spreading trenches [Heilweil *et al.*, 2015]. While the Green-Ampt and Bouwer models provide simple expressions to predict infiltration, the assumption of a homogenous isotropic soil limits scenarios where they can be applied. Specifically, none of the analytical models can represent a transient ponded infiltration scenario with vertically anisotropic soil.

2.5 Hydrus

While analytical and semi-analytical models exist to estimate flow in the vadose zone, many problems require a numerical model to represent complex, nonlinear physical processes. The U.S. Salinity Laboratory and the University of California, Riverside has developed numerous models over the last few decades to solve realistic problems of flow and transport in unsaturated media. These include UNSAT, SWMII, SWMS_2D and 3D, Chain_2D, UNSATCHEM_2D, Hydrus 1-D, and HP1 [Simunek *et al.*, 2008]. Hydrus is one of many numerical models developed to handle multiple non-linear processes for complex applications involving flow and transport in variably saturated media [Simunek and Bradford, 2008]. Hydrus 2D/3D incorporates components many of the earlier models, in addition to modules that represent more advanced scenarios, such as transport in a non-uniform flow system or complex boundary conditions.

Hydrus 2D/3D numerically solves the Richards equation for variably saturated flow across a linear finite element mesh. Options in Hydrus 2D/3D allow for representation of the following systems and processes: precipitation, evaporation, infiltration, runoff, lateral flow, soil water storage, capillary rise, deep groundwater recharge, hysteresis, root water uptake, and nonequilibrium flow [Simunek *et al.*, 2012]. Hydrus is also capable of solving advection-dispersion equations across linear finite elements for heat and contaminant transport. Hydrus 2D/3D is not limited to a specific spatial or temporal scale. Simulations can represent small-scale laboratory setups over just a few minutes to soil profiles hundreds of meters deep for thousands of years. However, when attempting to solve the highly nonlinear equations, 3D models with small spatial discretization can exceed current computing power [Simunek *et al.*, 2012].

Hydrus simulations have recently been applied to solve a wide range of flow and contaminant transport problems within the vadose zone. Many recent studies have developed Hydrus 2D/3D

models to compare agricultural practices, with a focus on optimizing water input and minimizing contaminants leached to the groundwater [Ebrahimian *et al.*, 2012; Finch *et al.*, 2008; Siyal *et al.*, 2012; Wang *et al.*, 2014]. Another application of Hydrus is to model field and laboratory experiments. Comparison of measured data from hundreds of laboratory experiments to Hydrus simulations showed that preferential flow can cause water to travel further than would have otherwise been predicted by the Richards equation [Germann and Hensel, 2006]. Hydrus models are also useful to predict effectiveness of a conservation practice. The measured soil moisture distribution following constant head irrigation was used to calibrate a 2D Hydrus model, which was used to test the impact of plowing treatments on infiltration [Akbar *et al.*, 2015].

A review of recent papers (2010-2018) showed hundreds of applications of Hydrus 2D/3D to simulate flow and contaminant transport in the vadose zone. Despite this, there was a dearth of documented cases where Hydrus was used to predict infiltration under ponded conditions with time-varying boundary conditions. Furthermore, there is a lack of studies using Hydrus models to predict measured field infiltration. The research presented here explores a novel approach using Hydrus 2D/3D to predict volumetric flow rate in the vadose zone in order to compare results to measured data.

2.5.1 Boundary Conditions

This section paraphrases a description of Hydrus boundary conditions from *Soil Physics with Hydrus Modelling and Applications* [Radcliffe, 2010].

Initial model conditions specify how Hydrus will solve the Richards Equation across the model domain. Solutions can be obtained in either water content (θ) or pressure head (h), with the latter as the preferred option since h drives water flow. A system-independent boundary, such as a Dirichlet or type-1 pressure head, can be applied when there is a known

head. This would include simulating ponded infiltration where there is a known hydrostatic pressure. In this scenario with known h , water flux across the boundary is calculated in Hydrus. Another system-independent boundary condition is a type-2 Neumann boundary with a known flux across a boundary. This boundary can be used if the flux across the boundary is independent of the rest of the system. One common type 2 boundary condition is a “free drainage” where the flux is specified to equal unit gradient conditions. While it may seem like a constant flux would represent precipitation, this is not the case. Hydrus represents ponding and runoff which are dependent on system properties that would reduce the total flux of water crossing the flux boundary.

In system-dependent boundary conditions, such as precipitation and evaporation, neither the head or flux is known. The boundary in this scenario is dependent on moisture conditions (if water is available to evaporate) and infiltration properties (precipitation may exceed infiltration capacity). Many additional boundary conditions have been developed in Hydrus to model various systems. Recent developments include a reservoir boundary condition that can be adapted to represent wells, furrows, and wetlands [Simunek *et al.*, 2018].

2.5.2 Rosetta

Vadose zone models such as Hydrus require hydraulic parameters of water retention and K_s . To directly measure the water retention variables described by van Genuchten and Mualem (Section 2.2), each soil sample would require laboratory analysis to solve an inverse solution within Hydrus. While this type of analysis has been noted to greatly improve physical models [Radcliffe, 2010], there is still a significant challenge in addressing the spatial variability that is often exhibited in soils. This common problem with unsaturated zone studies has led to the development of widely used pedotransfer functions (PTFs) that use simple measurements of soil

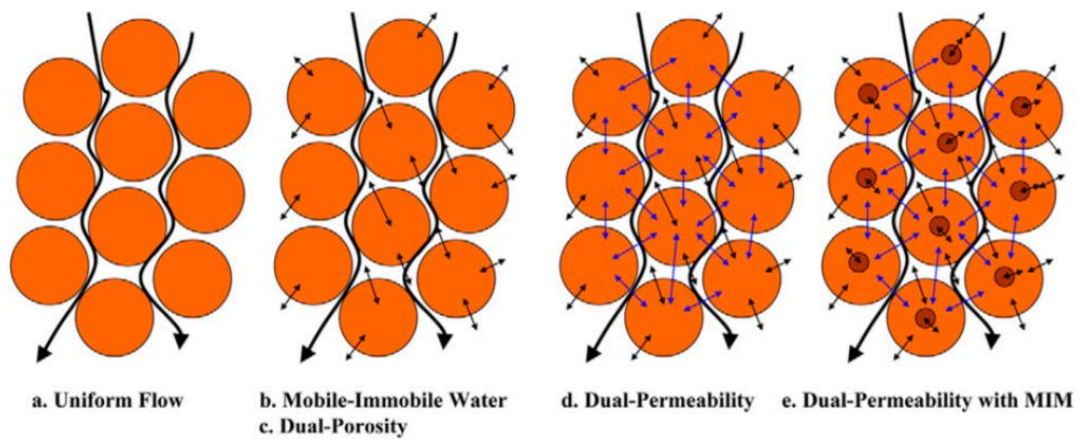
particle size distribution (PSD) and bulk density to predict soil hydraulic properties. The Rosetta model, developed by the U.S. Salinity Laboratory, predicts van Genuchten parameters using Mualem's pore size model (Section 2.2). Rosetta uses a neural network bootstrap method to estimate these parameters based on data from 2134 water retention samples and 1306 K_s samples [Schaap *et al.*, 2001]. Predictions can be made using only PSD data, but improved measurements have been observed when additional data such as bulk density and water retention are added [Schaap *et al.*, 2001]. Version 1.1 of Rosetta Lite was used within Hydrus to estimate the soil water retention parameters for this research.

2.5.3 Nonequilibrium Flow Models

Preferential flow allows water and contaminants to be rapidly transported through the vadose zone by bypassing parts of the matrix pore space, resulting in water travelling farther than would be predicted by the Richards Equation; many models have been developed to describe preferential flow models for various applications, but practical application remains limited due to the large number of parameters required to accurately depict the subsurface structure resulting in non-uniform flow [Simunek *et al.*, 2003]. By default, Hydrus uses the uniform flow model, where the Richards Equation dictates the rate at which water can flow through the pore space within an impermeable matrix (Figure 2.3a). Three nonequilibrium flow models have been created in Hydrus to address increasingly complex representation of physical and chemical flow through a model domain. The dual porosity model assumes that part of the flow domain water is immobile, and flow is restricted to fractures or macropores (Figure 2.3b/c). Water can move into the soil matrix via advection and diffusion but cannot move between soil aggregates. The dual permeability model allows for flow between soil aggregates within the soil matrix (micropores). This effectively assumes there is one fast-flow domain through the macropores, and one slow-flow domain through the micropores (Figure 2.2d). The dual permeability with (MIM) builds on

the dual permeability model by assuming that there is an additional area within the matrix that water can enter through molecular diffusion (Figure 2.2e). While models of increasing complexity may do a better job representing the physical processes within the soil, it can be difficult to directly measure many of the parameters required to run non-equilibrium models [Simunek and van Genuchten, 2008].

Figure 2.2 Figure from Simunek and van Genuchten [2008] displaying flow models of increasing complexity that can be applied in Hydrus 1-D.

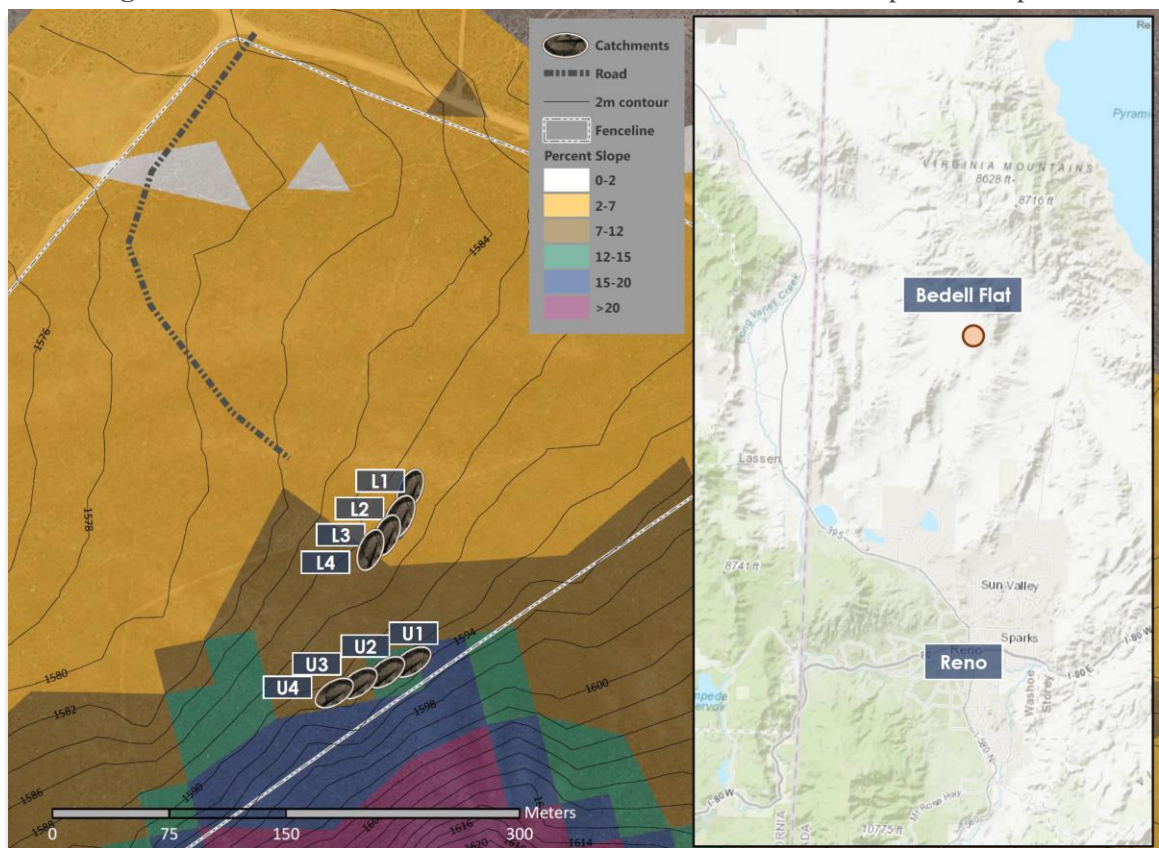


3 Methods

3.1 Site Description

Field investigations were carried out at a Bureau of Land Management (BLM) experimental research site at Bedell Flat northeast of Reno, Nevada (Fig. 3.1). Eight total MCs were created in two transects along a contour with varied slope conditions. The lower sites (L1-L4) had slopes of 5 to 8 percent, while the upper sites (U1-U4) ranged from 10 to 15 percent slope.

Figure 3.1 Overview of Bedell flat area with locations of MCs and percent slope.



The hillslope of the study area soil was primarily composed of the Bedell Series, with a taxonomic class defined by the NRCS as a coarse-loamy, mixed, superactive, mesic Aridic

Argixeroll [NRCS, 2017]. Both upper and lower sites were on a gently sloping pediment and are considered well drained with a medium runoff class and low water storage. The underlying bedrock is typically within 1-2 m of depth is mapped by the USGS as a Cretaceous granodiorite. A typical soil profile is presented in Table 3.1:

Table 3.1 Typical pedon description of Bedell Series [NRCS, 2017].

Horizon	Structure	Depth (cm)	Texture
A1	medium subangular blocky	0-3	loamy sand
A2	medium and coarse subangular blocky	3-38	loamy sand
Bt1	massive	38-61	sandy loam
Bt2	massive	61-137	sandy loam
C	massive	137-165	loamy coarse sand

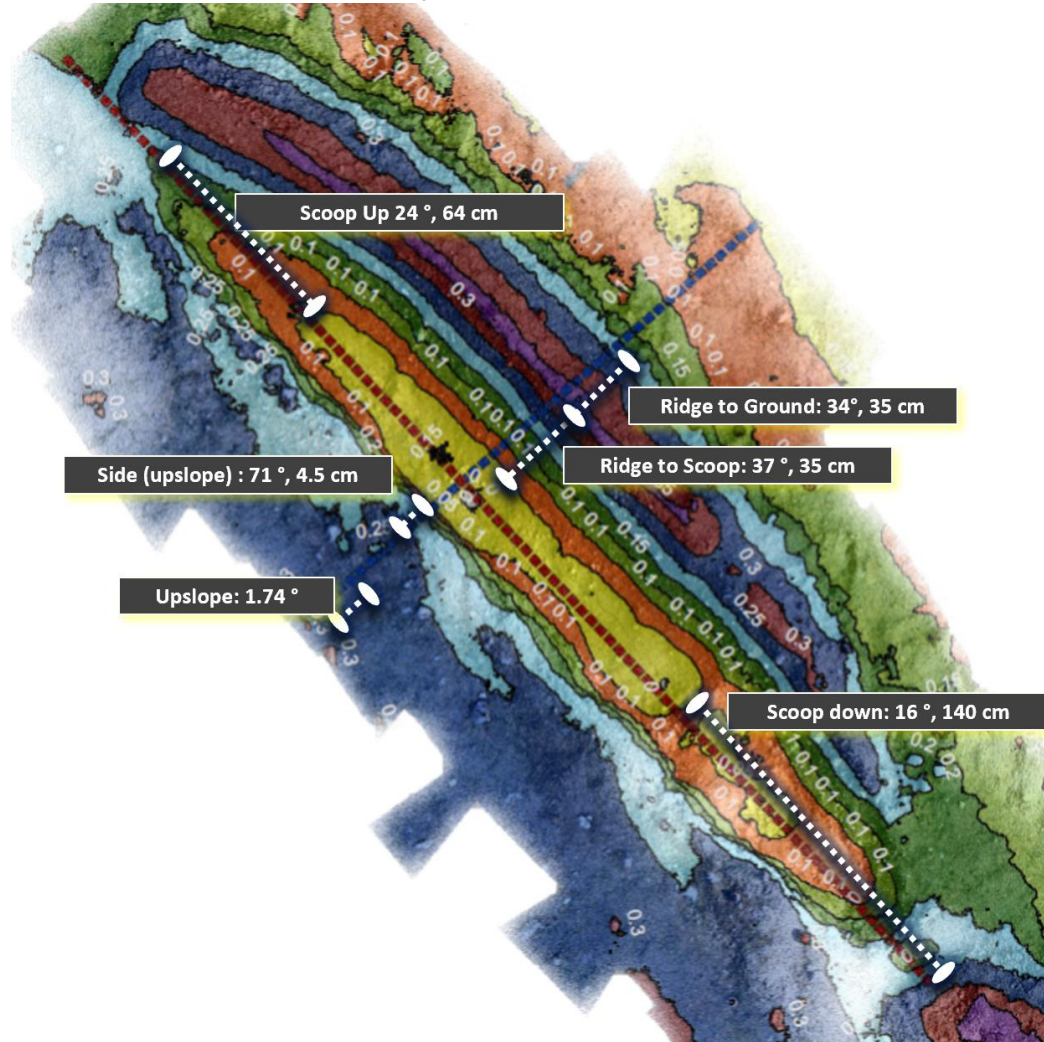
The soils had a relatively similar texture with depth. However, illuvial silica has been observed discontinuously in the lower soil horizons [Blank, 2018]. Increased illuvial silica can form a flow barrier in the subsurface similar to a duripan. While no duripan has been observed at Bedell, the illuvial silica could be restricting flow in some areas.

3.2 Micro-catchment Design

Eight MCs were plowed perpendicular to the slope by a small tractor pulling two offset plow shovels on July 14, 2017. The maximum depth reached by the tractor and shovel plows was limited to about 20 cm, and each catchment had to be manually shaped to representative dimensions of MCs that would be constructed by a Vallerani Plow in an operational scenario. A 3D model of a MC created by a Vallerani Plow in Jordan [Strohmeier, 2017] was used to design the shape of the Bedell Flat MCs (Figure 3.2). The following process was used to refine the MC morphology prior to simulations:

- Catchments were shaped so that the length from the beginning of scoop-down to the edge of the berm was 350 cm.
- The upslope wall of the catchment was reshaped using a square point shovel to an angle ranging from 80-90 degrees.
- The downslope berm of a MC was created when soil is pushed out by the plow. Additional soil was shoveled from the MC pit onto the berm. The soil would naturally settle until the berm was at the angle of repose for unconsolidated soil. This was consistently 35-45 degrees on each side of the berm for MCs created in the field and for MCs created by a Vallerani plow in Jordan (Fig. 3.2). Each MC's berm held at a similar angle of about 35 degrees.
- The berm began about 10 cm (lengthwise) after the scoop-down. This allowed for a pathway for water to flow out of the catchment without directly causing erosion of the berm structure. This was done to match the example MC from Jordan and was consistent with the description of the Vallerani System process.
- Each catchment was excavated down to 30-32 cm for the 150 cm centerline of the catchment (not part of scoop down or up). Once leveled, a digging bar was used to break up the ground an additional 10-15 cm along a 20 cm wide furrow along the centerline of each MC to approximate the ripper of the Vallerani Plow System.
- Prior to the simulations, each catchment was reshaped and leveled to a bottom depth of 30 cm.
- It is expected that the construction process resulted in MC morphology similar to that of one created with a Vallerani Plow.

Figure 3.2 MC morphology created from 3-D model sent from Jordan showing recently constructed MC by Vallerani Plow [Strohmeier, 2017].



3.3 Micro-catchment Instrumentation and Sampling

Rainfall and concentrated flow (CF) simulations were carried out August 1, 2017 through August 10, 2017. Each of the eight MCs required a full day to complete the series of simulations. The experimental design is broken into the following sections detailing catchment instrumentation and sampling: MC instrumentation, soil measurements, DEM generation, rainfall simulations, and concentrated flow simulations.

3.3.1 Micro-catchment Instrumentation

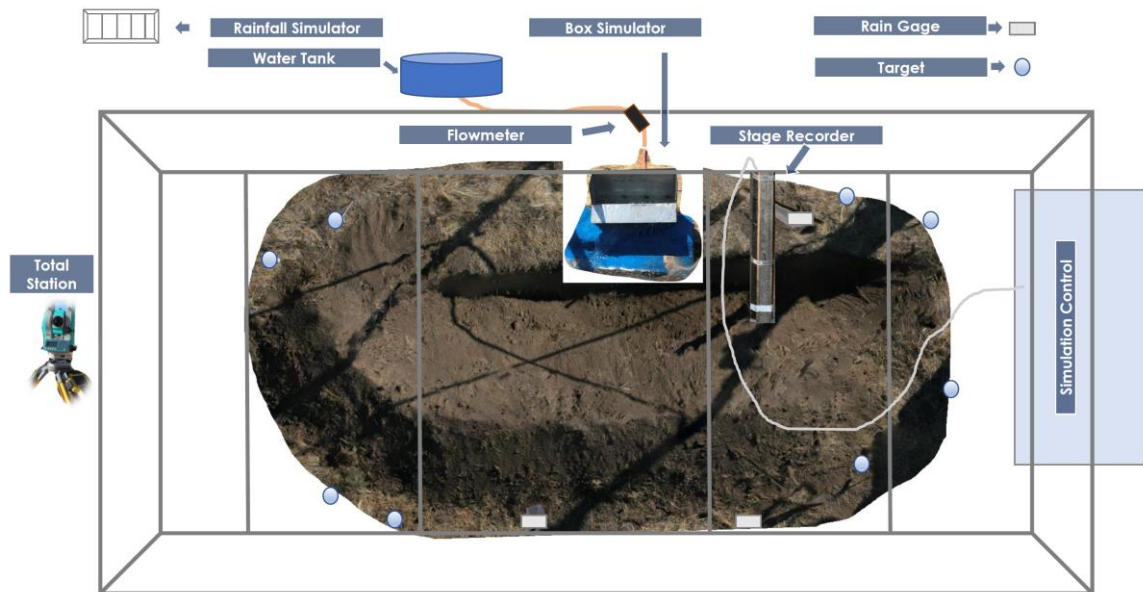
The following describes the instrumentation set up around each MC (Fig. 3.3).

- Final shaping of MC was carried out to make sure its geometry was correct.
- The variable intensity Walnut Gulch Rainfall Simulator (WGRS) applied rainfall from a single oscillating boom to a 2 m by 6.1 m area [Paige *et al.*, 2004]. The WGRS was set up over each MC with three nozzles aligned so that they spanned the length of the MC (the fourth nozzle was plugged).
- A simulation control station was set up with a field computer that controls the WGRS and two pressure transducers that were used to measure ponded depth. One transducer was an ISCO® Bubbler which was connected to the custom-built stage recorder (SR) described below. The second was a vented KSPI 700 Level Transducer (KPSI) placed within the SR.
- Eight visual targets were placed around the MC to serve as fixed markers for a Nikon NPR 352 total station. The process to survey these targets for 3-D model development in each MC is described in Section 3.2.3.
- Three standard rain gages were placed around the MC. Gages were recorded after each rainfall simulation.
- A custom-built SR device was constructed out of a perforated, 8.8 cm diameter PVC pipe. A ruler was clamped to the outside of the PVC pipe to act as a staff plate. An adapter for the ISCO bubbler was placed within the PVC pipe with tubing to record pressure at the bottom of the catchment. The KPSI transducer was placed inside the PVC pipe so that it also rested at the bottom of the SR. The final SR had two continuous pressure transducers and a staff plate to monitor stage within the MC. The SR was placed

at or near the minimum elevation within the catchment. The staff plate was level with the bottom of the catchment.

- After rainfall simulations, a box simulator (defined in Section 3.3.1) was set up in an upslope position (Fig. 3.3) to provide concentrated flow simulations.

Figure 3.3 MC instrumentation with WGRS, box simulator, and SR.



3.3.2 Soil Measurements and Sampling

The purpose of this research is to use simple soil measurements with a Guelph Permeameter (GP) to predict more complex infiltration dynamics within MCs. A GP was selected as the primary measure of soil physical properties because readings can be made quickly and at varied depths. The minimum depth recommended by the manufacturer (Soilmoisture Equipment Corp.) is 15 cm. GP measurements were carried out at depths of 15 cm, 25 cm, 35 cm, 45 cm, 55 cm, and within the MC berm. All wells were created with a 6 cm diameter soil auger and brushed with a well brush auger. GP measurements were taken in a transect on each side of MCs (Fig. 3.4). All measurements were taken with the GP set to 10 cm of head ($H=10$), which allows water to rise

within the well to 10 cm. Each well had a radius of 3 cm ($a=3$). The steady state water level change was recorded at minute intervals for 10-25 minutes. After three recordings of a steady rate of water level fall, the GP measurement was considered complete. Guelph Permeameter data was collected over two periods. The first set of data was collected in September 2017 during rainfall and concentrated flow simulations. A second set of data was collected in 2018 to provide a more complete set of data and to understand the variability in K_s at depth. The 2017 dataset had many gaps where there was only one measurement at a certain depth, and was incomplete below 35 cm. The 2018 dataset was a complete set of measurements to 55 cm on both sides of each MC, and within the berm. GP calculations used the parameter values listed in Table 3.2.

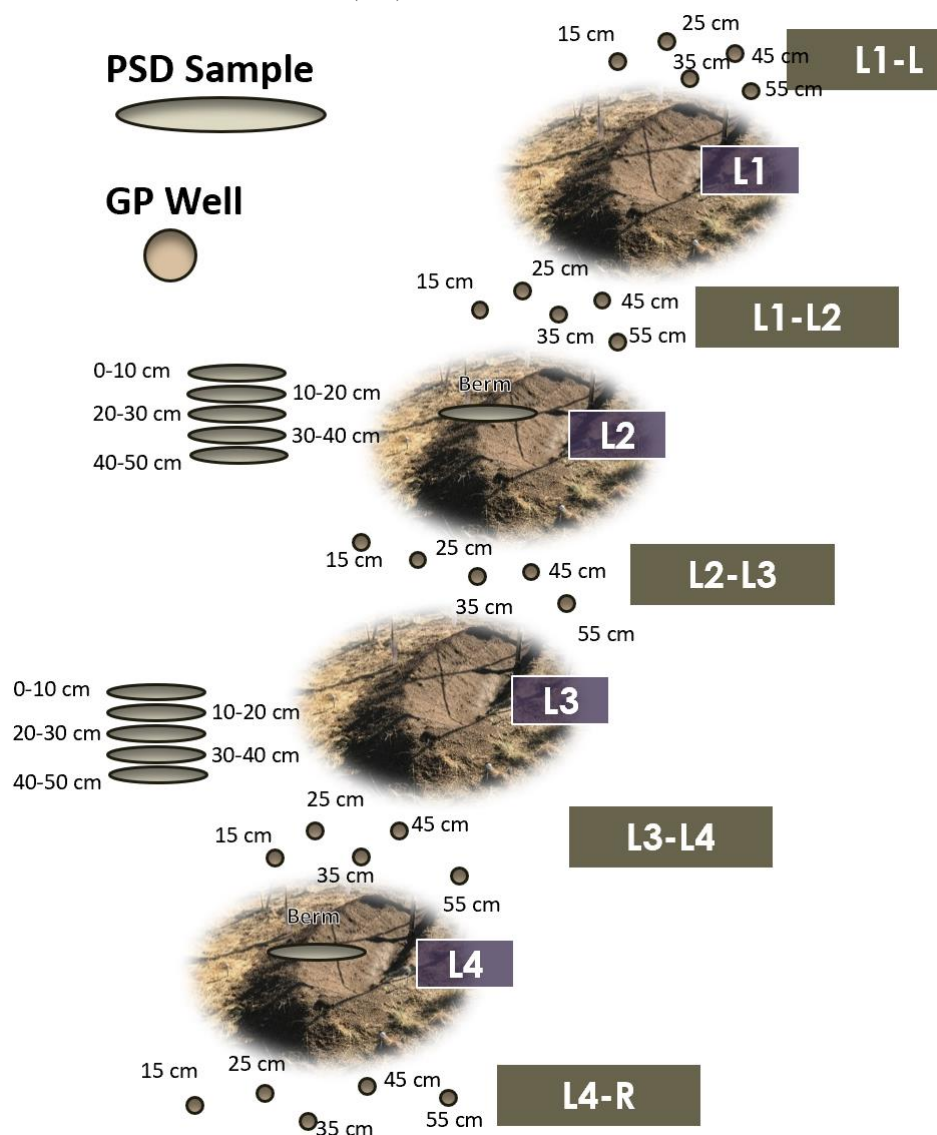
Table 3.2 Values used for GP calculations.

H (cm) – Height of ponded water	10
α^*	0.12
a (cm) – well radius	3
Cross-sectional area (cm²)	35.22
π	3.1416
Shape Factor C	1.29

Soil samples were also collected to complete laboratory measurements of bulk density and soil particle size distribution (PSD). PSD samples were collected at five depths, from the soil berm, and bottom of the pit following rainfall (Fig. 3.4). Two of the sites were in the lower set of MCs and two were in the upper. Measurements of bulk density and PSD were processed in the Great Basin Rangelands Research Unit Soils Laboratory of the USDA Agricultural Research Service. The average bulk densities at the soil surface were 1.306 g/cm³ and 1.366 g/cm³ for upper and lower sites respectively. The Rosetta Lite 1.1 Neural Network tool included in Hydrus 2-D was used to predict saturated and unsaturated hydraulic conductivity parameters according to the models of van Genuchten and Mualem [*Schaap et al.*, 2001]. Bulk density was not included in

this estimate since it was only collected at the soil surface. PSD data for two samples at each depth interval were collected for upper and lower sites.

Figure 3.4 Schematic overview of soil particle size distribution (PSD) sampling and Guelph Permeameter (GP) measurements for lower MCs.



3.3.3 Structure from Motion

A 3-D model of each MC was created using structure from motion (SfM) techniques with Agisoft PhotoScan software. The following describes the process used to create a set of 3-D

digital elevation models before and after a series of rainfall events described in Section 3.4. By comparing DEMs created before and after rainfall events, it is possible to measure erosion and deposition between each rainfall event. For the purposes of this effort, only the DEMs created following the second rainfall event on each MC were utilized to create stage to volume relationships.

- Eight fixed control targets placed around each site were surveyed with a Nikon NPR 352 total station to accurately project SFM models in space.
- Over fifty photos were taken with a Canon Rebel XTi and an iPhone 7 between each rainfall simulation at each site. The set of photos from both cameras were used to develop accurate SFM models. Photos were taken at the following times: prior to the rainfall event, after the first rainfall event, following the second rainfall event, and after the concentrated flow experiment. The four rounds of SFM at each site with both cameras totaled 64 sets of photos that were subsequently developed into digital elevation models (DEM's), each representing a snapshot in time.
- Agisoft PhotoScan software was used to align photos, build a dense point clouds, and input control points. The resulting DEM's were accurate to within 0.5 cm.
- DEM's for each MC were exported to Esri ArcMap 10.4.1.

3.3.4 Micro-catchment geometry

Digital elevation models created for each MC were used to establish relationships between stage, volume, and 3-D surface area. The 3-D surface area considers the topography within the catchment (not planar) and is multiplied by the water velocity to calculate volumetric flow rates. The data to create this relationship was exported from the DEMs created following rainfall events for each site in ESRI ArcMap using the Surface Volume tool across a range of depths. The

Surface Volume tool was used at 14 to 18 levels within the MC to adequately characterize the geometry. These datasets were imported into Microsoft Excel where polynomial relationships were applied to relate stage in each MC to surface area or volume.

3.4 Rainfall Simulations

The field experiments were carried out between August 1st-10th, 2017. Two rainfall simulations followed by the concentrated flow simulations were completed on each site (L1-L4, U1-U4). A Walnut Gulch Rainfall Simulator (WGRS) was used to simulate two rainfall events over each MC. These rainfall simulations were used to simulate natural conditions within the MCs because:

1. the impact of raindrops has been observed to cause surface sealing of soils which affects infiltration properties [Assouline and Mualem, 2002], and
2. changes in water content alter hydraulic conductivity throughout the soil profile (Section 2.2) and the simulations set realistic soil moisture conditions for the concentrated flow simulations.

The rainfall intensity and duration for both runs at each site are listed in Table 3.3. Following each rainfall simulation, the catchment would be allowed to dry so that SFM photos could be taken. The ponded levels following rainfall application sometimes took upwards of two hours to drain.

Table 3.3 Rainfall intensity, duration, and total rainfall applied to each MC.

Site ID	Run 1		Run 2		Total Rainfall (cm)
	Intensity (cm/hr)	Duration (min)	Intensity (cm/hr)	Duration (min)	
L1	15.24	5	15.24	5	2.54
L2	10.16	5	10.16	10	2.54
L3	15.24	5	15.24	15	5.08
L4	10.16	5	10.16	10	2.54
U1	15.24	5	15.24	15	5.08
U2	10.16	5	10.16	25	5.08
U3	15.24	5	15.24	5	2.54
U4	10.16	5	10.16	10	2.54

3.5 Concentrated Flow Simulation

The concept behind the concentrated flow (CF) experiment was to study infiltration dynamics within MCs so that the system could be accurately modeled to predict infiltration rates near MC capacity. Concentrated flow into MCs has been observed to exceed catchment infiltration capacity causing catchments to fill and further concentrate flow downslope [Oweis et al. 2011]. This can potentially cause erosional failure of downslope MCs. Given the focus on erosion within the UCRB, restoration treatments must be designed so that they are unlikely to fail. This experiment represents a scenario where a hillslope received a large amount of rainfall which is represented by the rainfall simulations carried out prior to concentrated flow simulation. The large rainfall rate exceeds the infiltration capacity of the upslope soil resulting in runoff entering the MC. To deliver the water from upslope, we used a “box simulator” also known as the “rill-simulator”. The simulator has previously been used in experiments studying rill formation. The design of the simulator is a simple stainless-steel box connected to a hose and a pump with a pressure regulator to control flow rate. The energy of the water coming in is dissipated within the box as it fills up. After just a few seconds, the water flowed over the lip of the box simulator onto an Astroturf mat and into the catchment. The Astroturf was placed on the upslope edge of the MC

to dissipate erosive forces of water entering the catchment. A GPI industrial grade electronic digital flowmeter rated from 2 to 20 gallons per minute was placed in the inlet to the box to measure the volume and flow rate going into the catchment. The following steps were carried out for each concentrated flow simulation:

- Each MC was allowed to dry out following rainfall simulations and prior to concentrated flow input. The time to dry was variable in each MC, but averaged about 140 minutes.
- A computer program was started to record continuous data from the pressure transducers (KPSI and Bubbler).
- The MC was filled with water as the flowrate into the catchment was kept steady. Once the water overtopped the catchment, the flowrate was maintained for an additional 15-45 minutes to observe if erosion of the berm occurred.
- The MC was continuously monitored by pressure transducers to record infiltration rates. The KPSI recorded stage at a one second intervals, and the Bubbler recorded every 5 seconds.
- Due to time constraints of field work, the MCs were not always allowed to drain completely. Experiments were generally stopped after about 120 minutes, or when the stage within the catchment dropped below 10 cm. This data was considered less important because the focus of this research is the infiltration rates of a MC near maximum capacity.
- In the upper site U2, a rodent hole was exposed near the bottom of the MC that caused rapid infiltration rates. Consequently, the data for U2 was not used to develop an infiltration model.
- The continuous SR data from the KPSI for each of the seven MCs (excluding U2) was averaged to one-minute intervals, where minute “1” averaged data between 30 and 90 seconds. This was done to simplify the data and smooth out any minor irregularities

occurring over small intervals. The volumetric flow rate (cm^3/min) was then calculated by subtracting the volume in a MC between each minute timestep.

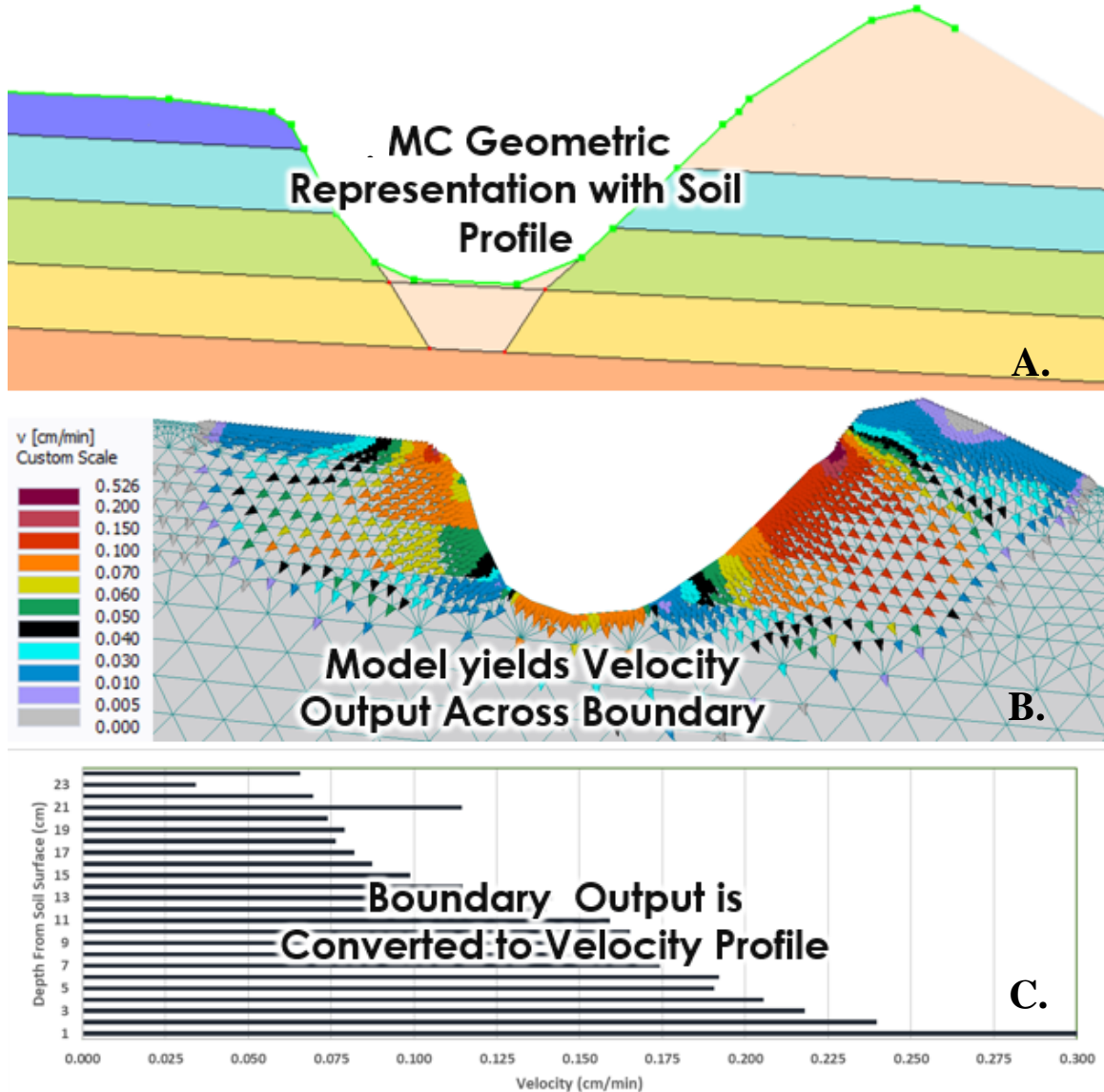
3.6 Micro-catchment Infiltration Model

A predictive model for micro-catchment infiltration was developed using Hydrus software for a cross-section of a MC. The goal of the model was to output a velocity profile from the soil surface to the bottom of the MC that could be output at a specified number of timesteps. This velocity profile could then be used in conjunction with stage to surface area relationships for each pit to calculate the total volumetric flow rate at a given timestep. The Hydrus model accounts for the following conditions:

- accurate cross-sectional representation of each MC,
- antecedent soil conditions,
- representation of the soil profile that can be parameterized with GP data,
- representation of the height of ponded water within each pit as a function of time,
- flexibility for future adaptation to more complex scenarios (i.e., longer duration, dual permeability, more complex soil, root or plant growth), and
- accounts for 3-D (radial) flow.

The following process was used to develop a MC predictive infiltration model. A representative cross section with adaptable soil profile was developed in Hydrus (Fig. 3.5a). The model was executed, yielding a velocity distribution across the saturated area (Fig. 3.5b). The boundary output information for relevant timesteps was averaged across each depth interval to create a vertical velocity profile with soil depth (Fig. 3.5c).

Figure 3.5 MC predictive infiltration model to yield velocity profile with soil depth.



The velocity profile provides useful information to convert 1-D flux of water q [LT^{-1}] into volumetric flow rate (Q) [L^3T^{-1}] using DEM relationships. The DEM data has been developed into relationships between stage in each MC and 3-D surface area and volume. The MC infiltration model calculates the 3-D surface area for each 1 cm interval from the soil surface to the bottom of the pit. The surface area is multiplied by the corresponding q value for the corresponding height interval. This yields a volumetric flow rate of water infiltrating into the MC

which can be summed over each height interval of the pit to yield a total flowrate (Q_{sum}) for a given timestep.

$$Q_{sum} = \sum_{MC\ bottom}^{Soil\ Surface} Q_{1\ cm\ interval}$$

3.7 Hydrus Model

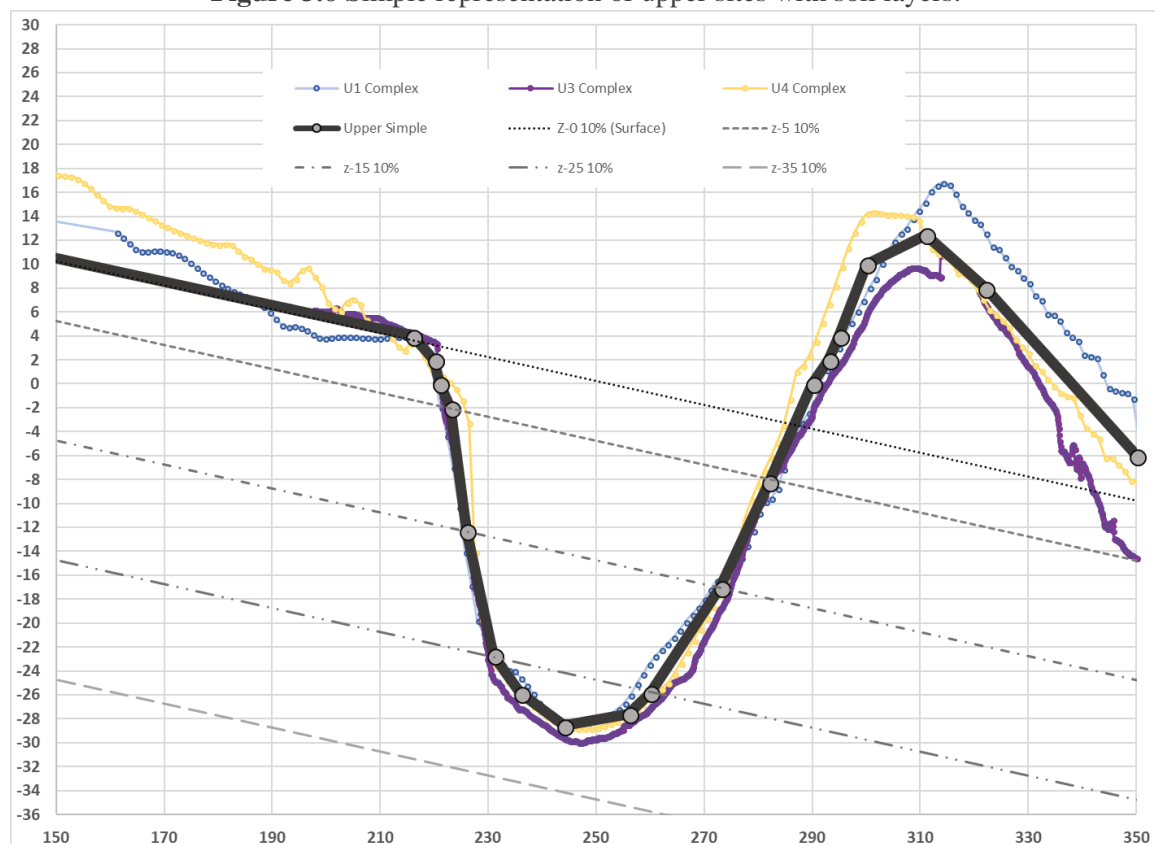
The following sections will describe a Hydrus model designed to capture the complex infiltration dynamics within a MC. The 2-D Hydrus model yields a velocity profile that can be output and multiplied by the surface area at each centimeter interval to calculate infiltration flux. The model was set up to represent the field studies so that at any given timestep the models predicted volumetric flow rate could be compared to measured volumetric flow rate in MCs (Section 4.4).

3.7.1 Hydrus Model Geometry

A representative cross-section from upslope across the berm of each MC was exported from the DEM for each MC. Each cross section was projected into space over one another. Two representative cross-sections were developed combining lower sites (L1, L2, L3, L4) and upper sites (U1, U3, U4) into two simplified geometries. A model domain was created that used the representative cross-sections parameterized by soil measurements made in the field. The slope measured in the field was incorporated into the model under the assumption that the soil measured at depths within the soil profile had the same slope as the soil surface (Fig. 3.6). This is a realistic assumption based on the lower conductivity layers observed at similar depths between field sites. The upper sites were modeled with a 10% slope, and the lower sites with a 5% slope. These layers were projected out 250 cm horizontally from a hypothetical surface point of “0”

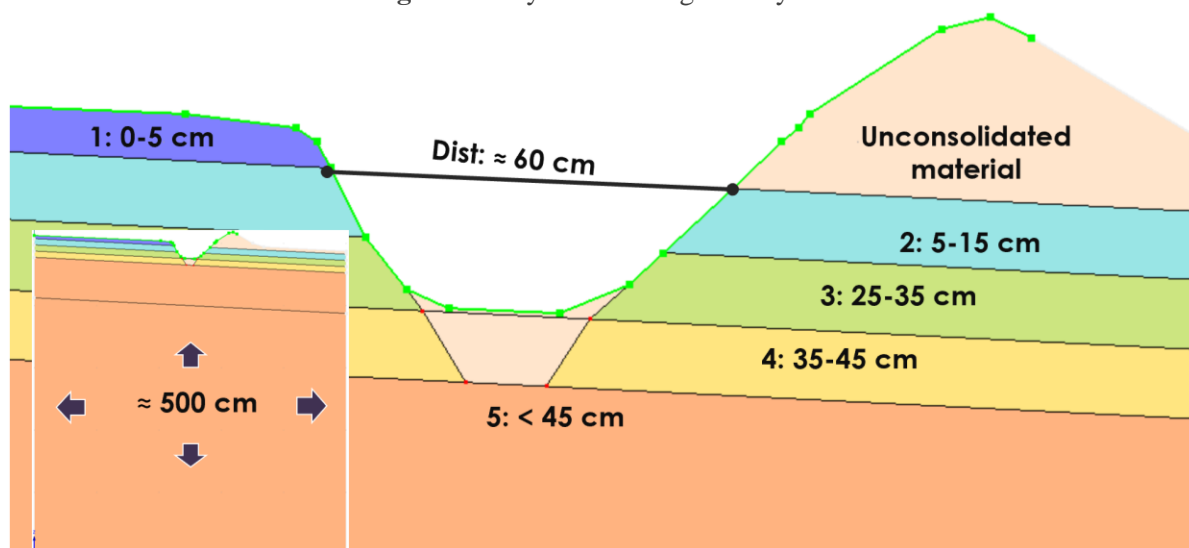
elevation located over the pit. Additional points were added to project the breaks in soil layers at the correct slope across the model domain. The simple model of geometry for upper and lower sites were then imported into Hydrus.

Figure 3.6 Simple representation of upper sites with soil layers.



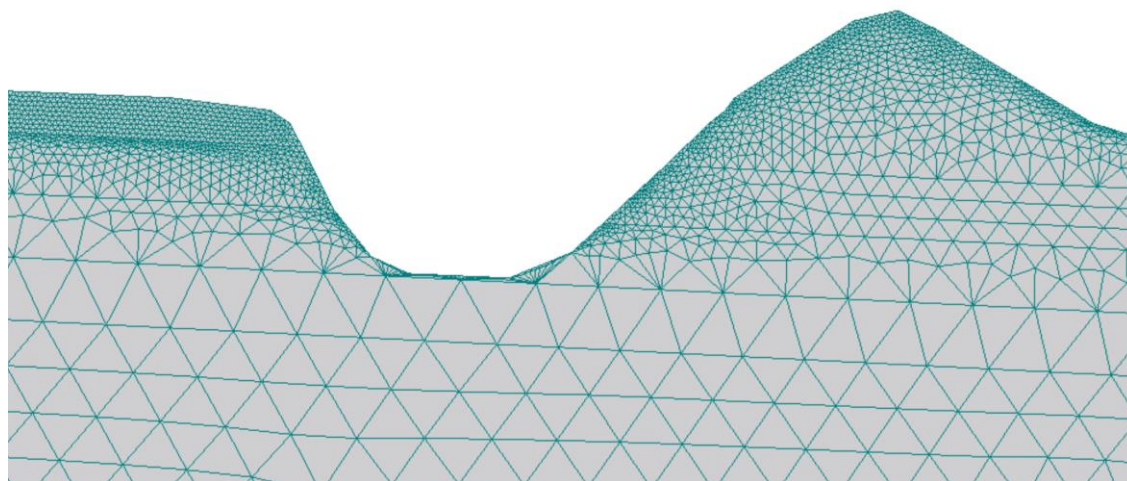
The model domain for upper and lower sites was approximately 500 cm wide by 500 cm tall. All the soil layers were manually drawn in Hydrus by connecting the imported points via polylines. Six soil types were specified for the berm material: 0-5 cm, 5-15 cm, 15-25 cm, 25-35 cm, 35-45 cm, and >45 cm (Fig. 3.7). The properties that were assigned to the berm were also specified for a wedge of soil at the bottom of the pit to represent how the digging bar created a 10 cm layer of unconsolidated material.

Figure 3.7 Hydrus model geometry.



Numerical solutions to the Richards equation require the model domain to be discretized. Hydrus 2D/3D includes MESHGEN software which can be used to create a finite element (FE) mesh. The targeted FE size was set to 10 cm. The soil surface was refined to 1 cm discretization to improve model function across the boundary between soil and air (Fig. 3.8). This also allowed for increased resolution in the model output across the area of interest. The FE mesh generated for the lower sites had 8,596 nodes and 16,297 2D elements. The upper sites FE mesh had 6,745 nodes and 12,796 2D elements.

Figure 3.8 Finite element mesh refinements.



3.7.2 Boundary Conditions

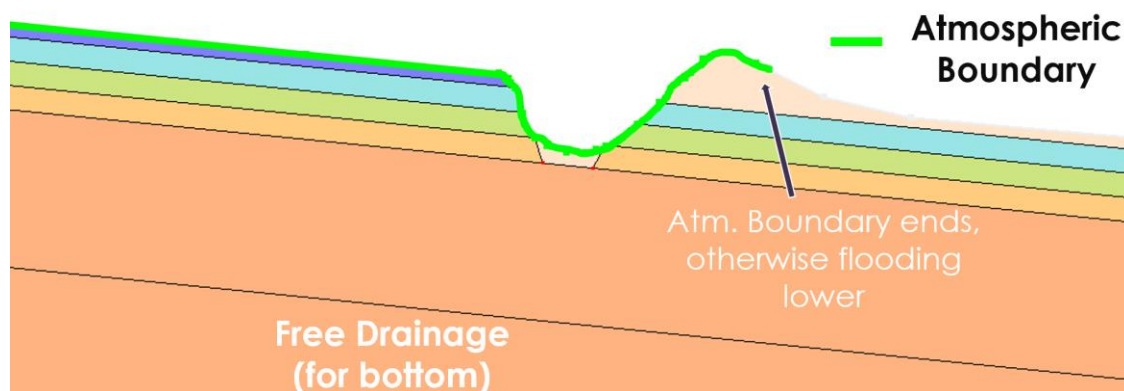
The bottom of a model was specified as free drainage. This was done in case the model is adapted to other scenarios but was not necessary in this case since moisture never came near 500 cm depth. An atmospheric boundary condition was applied from the upslope edge of the model to just past the ridge of the berm (Fig. 3.9). The boundary condition was not extended downslope of the berm to avoid allowing the boundary to drop below the maximum height of the ponded water in the pit. This would cause flooding to occur on the downslope side of the berm, which was not filled with water. The atmospheric boundary allows for precipitation, evaporation, and for the time varying head boundary to occur in the same location.

Evapotranspiration (ET) is only a small component of the flow budget over the short time period of the simulation. No ET was measured during the simulation. However, it is a necessary part of many hydrologic studies, and was accounted for in the Hydrus Model. Estimated ET rates for a similar site to Bedell Flat were taken from a USGS publication *Rates of Evapotranspiration, Recharge from Precipitation Beneath Selected Areas of Native Vegetation, and Streamflow Gain and Loss in Carson Valley, Douglas County, Nevada, and Alpine County* [Maurer et al., 2006]. The comparable site taken from the USGS report was also not irrigated and the depth to the water table was 1.8 m. The dates measured at the site ranged from Oct 2003-Oct 2004. The selected dates for ET were chosen for our field site between August 1st-10th, yielding an average ET of 0.203 cm/day. The evaporation rate is applied continuously over the simulation whenever the pressure head is negative.

Hydrus rainfall inputs were intended to mimic the initial conditions at the experimental site. Each Hydrus model had 2.54 cm of rainfall occurring over 60 minutes across the atmospheric boundary condition. After the first 60 minutes of rainfall, no water inputs are added to the simulation until

minute 200. This was to represent the time from when we operated the rainfall simulator to when we were able to begin the concentrated flow simulations.

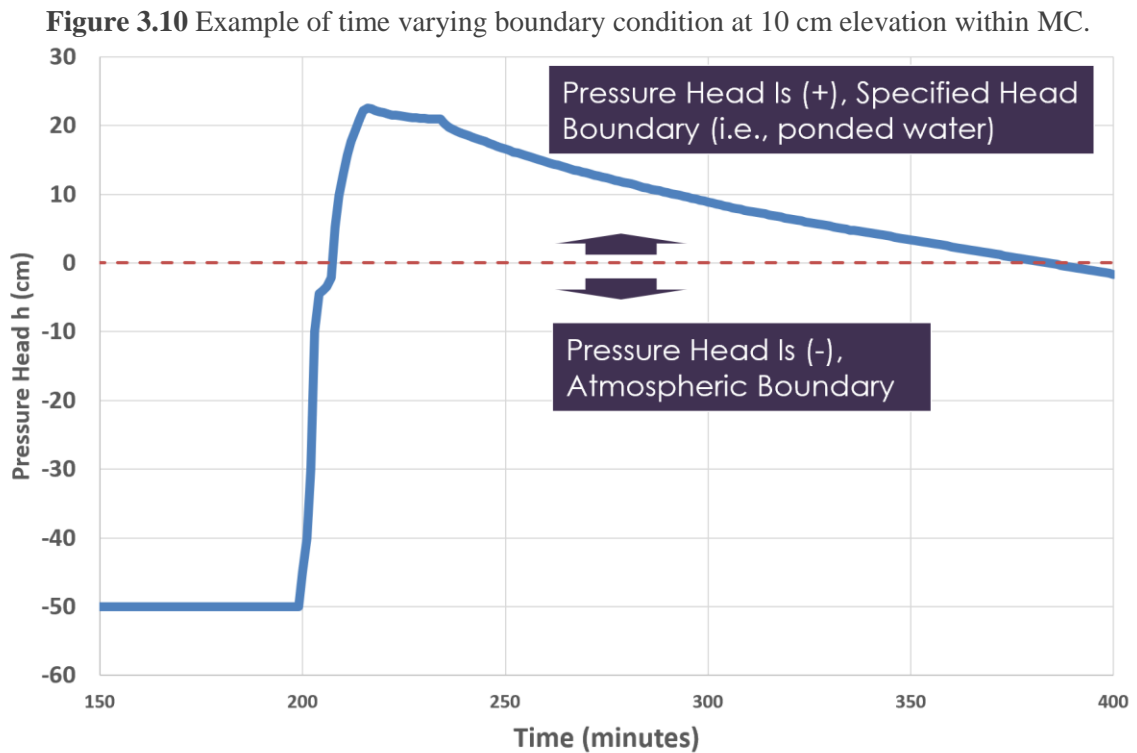
Figure 3.9 Hydrus model boundary conditions.



A time varying head boundary was used to simulate the height of ponded water within each MC. Hydrus references the positive variable pressure head boundary to the minimum elevation in the boundary condition. For example, with a minimum elevation of 0 and a pressure head (h) of 14 cm, a point at 10 cm of elevation would experience 4 cm of ponded water. The h values were pulled directly from the SR readings and projected into each MC model for upper or lower sites. This was accomplished by setting relationships between the observed maximum water level in the MC to the same level in the simplified Hydrus model. The result was a time varying pressure head boundary representing the exact height of ponded water specific to each site.

The option to have an “atmospheric boundary condition when the specified nodal pressure head is negative” was also selected. This implies that any time that there is negative pressure head (no ponded water $-h$) an atmospheric boundary condition is present. For the first 200 minutes of the simulation, the time varying head boundary was set to -50 cm. During this period, precipitation and evaporation can occur across the entire atmospheric boundary. The values representing the water input into the catchment began at 200 minutes into the simulation, after which the observed height of ponded water was applied to the entire boundary. Areas with positive h will have

ponded water while areas with negative h retain an atmospheric boundary. An example of the pressure head experienced at a single point 10 cm above the MC bottom is displayed in Figure 3.10. Note that the positive values where the specified head boundary are applied do not begin until about 205 minutes when the water within the MC rises above that point.



3.7.3 Hydrus 2-D Model Development

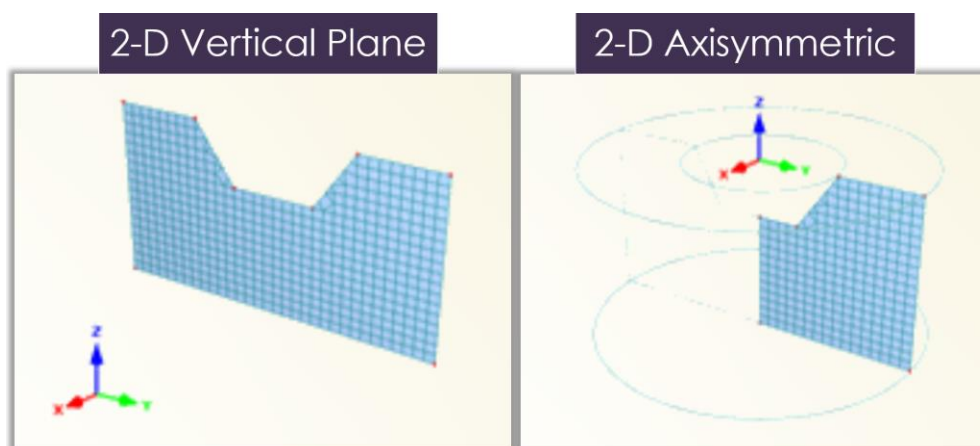
The Hydrus 2D model was set up in the vertical plane XZ dimensions to simulate water flow. The simulation was set up to run for 400 minutes with an initial time-step of one minute. Forty output timesteps were selected, with higher temporal resolution around the 200-minute mark when infiltration rates will be compared to measured data. Initial model conditions were specified in pressure heads to match measured data. The shape of the SWRC was defined by the van

Genuchten – Mualem hydraulic model with no hysteresis, and water flow parameters were originally specified based on measured PSD data for each depth interval.

3.7.4 Hydrus 2-D vs Axisymmetric Model Comparison

All models described previously were developed as 2-D vertical planes (Figure 3.11). This was done to create a cross-section that represented MC geometry. However, the vertical plane model ignores that water fluxes into the MC occur in 3-D. As water flows outwards in 3-D, there is increasing space for the water to flow into. This could be conceptualized using a 3-D Hydrus model, but that would have the disadvantage of not being translatable to variable geometry applications. 3-D flow can also be conceptualized as a 2-D axisymmetric model, allowing the entire model domain to be rotated along the z-axis. In this situation a smaller radius allows for much larger area for water to flow into. With a large radius, the flow outwards essentially is the same as a vertical plane. The question becomes what is the velocity profile difference between a 2-D vertical plane model and a 2-D axisymmetric model for the characteristic MC geometry? This was tested for a common MC shape.

Figure 3.11 Comparison of 2-D Vertical Plane and 2-D Axisymmetric model domains



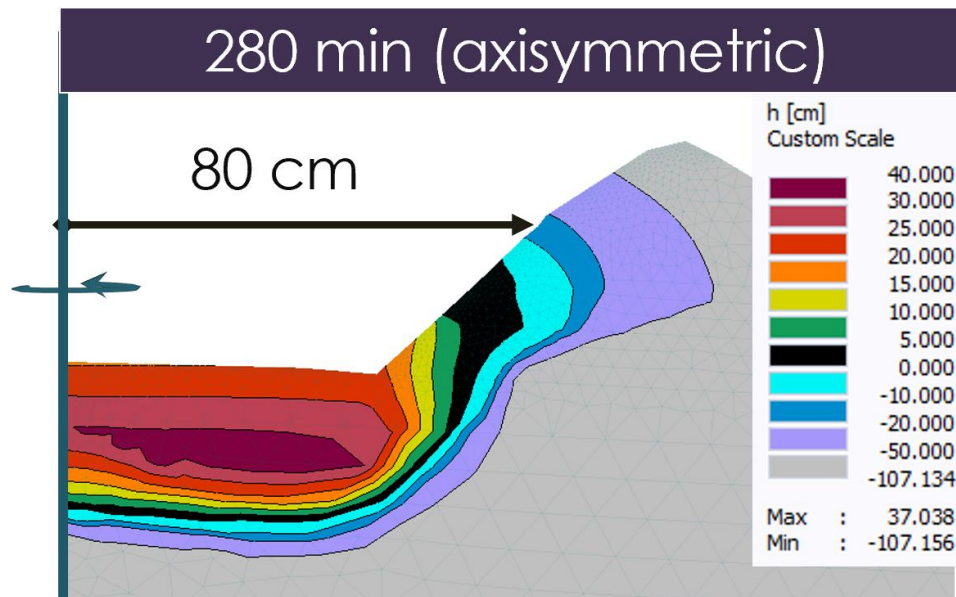
Model domain screenshots from Hydrus 2D/3D Version 2.05

The difference between 2-D vertical plane and 2-D asymmetric flow is dependent on the radius of the boundary being rotated. While MCs are not circular, the effective radius of a MC can be calculated below:

$$Effective\ Radius = \sqrt{\left(\frac{VMC\ Surface\ Area}{\pi}\right)}$$

For an average MC nearly full, the average effective radius was 80 cm. The MC Hydrus model was modified to have only one side that extends 80 cm and could be rotated along the z axis (Fig. 3.12). The model was run with two model domains. The original was run as a 2-D vertical plane model, just like each other MC model. The same geometry was then run as an axisymmetric model.

Figure 3.12 Comparison of 2-D Vertical Plane and 2-D Axisymmetric model domains.



3.7.5 Conductivity Profiles

The van Genuchten – Mualem hydraulic model requires inputs for both water retention parameters along with K_s . Water retention parameters (Q_r , Q_s , Alpha, n , I) were held constant for each simulation and were based on predictions from PSD data for each site (Table 4.1). Due to the high variability observed in the K_s data, the following models of K_s with depth were used in simulations for each site:

K_s Profile 1: PSD data was used in Rosetta to predict both water retention and K_s . The pairs of PSD measurements taken at the lower and upper sites were averaged (Table 4.1).

K_s Profile 2: For 0-35 cm, the 2018 GP dataset was used. The measurements on the two GP wells adjacent each were averaged (Table 4.3). For > 35 cm, the PSD data describe in K_s Profile 1 was used.

K_s Profile 3: GP data from 2018 was averaged for the two wells adjacent each MC for the entire soil profile (Table 4.3).

K_s Profile 4: The maximum GP measurement from each depth interval is selected from the GP datasets for the lower sites and upper sites. The two maximum values from the upper and lower sites at each depth interval are then averaged (Table 4.4). The model uses a single averaged K_s profile for all sites, regardless of hillslope position.

Running the seven MC models with four K_s profiles yielded 28 Hydrus solutions to compare to measured infiltration rates. The outputs could be compared at any timestep of interest. The period of interest for this study was the 30 minutes after inflow to each MC was stopped, allowing for observation of hydrologic function while the stage within the MC is near the maximum.

4 Results

4.1 Soils Analysis

The average of the samples of PSD at upper and lower MCs, along with Rosetta predictions of water retention parameters and K_s , are presented in Table 4.1.

Table 4.1 PSD data analysis and Rosetta Lite 1.1 neural network prediction of hydraulic parameters.

Site	Measured PSD Data					Rosetta Lite 1.1 Neural Network Prediction				
	Depth Interval	% Clay	% Silt	% Sand	Texture	Residual Water Content (Q_r) [cm ³ /cm ³]	Saturated Water Content (Q_s) [cm ³ /cm ³]	Alpha [1/cm]	n [-]	K_s [cm/min]
Lower	Avg Lower	8.7	15.1	74.9	Sandy Loam	0.042	0.384	0.038	1.5	0.042
	0-10 cm	3.1	15.0	81.5	Loamy Sand	0.037	0.389	0.044	1.8	0.084
	10-20 cm	6.2	13.8	79.2	Loamy Sand	0.041	0.385	0.040	1.6	0.061
	20-30 cm	11.4	15.9	71.3	Sandy Loam	0.046	0.383	0.035	1.4	0.031
	30-40 cm	11.9	15.6	70.7	Sandy Loam	0.046	0.383	0.034	1.4	0.029
	40-50 cm	10.9	15.0	71.9	Sandy Loam	0.045	0.383	0.035	1.4	0.033
	Basin	9.2	17.4	72.2	Sandy Loam	0.042	0.385	0.037	1.5	0.037
Berm	5.8	16.0	77.7	Loamy Sand	0.039	0.386	0.041	1.6	0.056	
Upper	Avg Upper	4.5	9.5	85.7	Loamy Sand	0.046	0.427	0.039	2.0	0.207
	0-10 cm	2.2	7.9	89.7	Sand	0.045	0.384	0.039	2.6	0.235
	10-20 cm	3.4	10.7	85.7	Loamy Sand	0.042	0.385	0.040	2.1	0.130
	20-30 cm	4.4	10.2	85.1	Loamy Sand	0.044	0.383	0.039	2.0	0.116
	30-40 cm	6.2	10.6	82.8	Loamy Sand	0.044	0.382	0.038	1.8	0.084
	40-50 cm	8.2	6.4	84.7	Loamy Sand	0.051	0.377	0.033	1.9	0.093
	Basin	4.0	11.1	84.1	Loamy Sand	0.042	0.385	0.040	2.0	0.112
Berm	3.1	10.4	85.6	Loamy Sand	0.042	0.386	0.041	2.1	0.131	

Tables 4.2 and 4.3. present GP data averaged from each side of a MC, if available. All K_{fs} values were calculated using the single head measurement method with equation 10 from Section 2.3.

Table 4.4 presents the maximum GP measurement at each depth interval averaged for upper and lower sites.

Table 4.2 2017 GP K_{fs} results averaged from wells on each side of a MC (cm/min).

Depth (cm)	L1	L2	L3	L4	U1	U3	U4	Lower Avg	Upper Avg	All Avg
5-15	0.039	0.027*	0.065*	0.083	0.138	0.063	0.026	0.053	0.076	0.063
15-25	0.031	0.038*	0.069*	0.069	0.073	0.127	0.046	0.052	0.082	0.065
25-35	0.023	0.014*	0.060*	0.062	0.092	0.087*	0.078*	0.040	0.086	0.059
35-45	-	0.003*	-	-	-	-	-	0.003*	-	-

*indicates data was only available on one side of MC, GP data from L2-L3 missing for all depths, U3-U4 missing for depth below 15 cm. Only L1-L2 was available below 35 cm.

Table 4.3 2018 GP K_{fs} results averaged from wells on each side of a MC and within berm (cm/min).

Depth (cm)	L1	L2	L3	L4	U1	U3	U4	Lower Avg	Upper Avg	All Avg
5-15	0.037	0.036	0.031	0.036	0.061	0.100	0.097	0.035	0.086	0.057
15-25	0.014	0.012	0.014	0.016	0.053	0.052	0.072	0.014	0.059	0.033
25-35	0.013	0.005	0.002	0.001	0.020	0.002	0.016	0.005	0.013	0.008
35-45	0.018	0.005	0.003	0.001	0.012	0.007	0.008	0.007	0.009	0.008
45-55	0.006	0.006	0.006	0.004	0.012	0.001	0.004	0.005	0.006	0.005
Berm	0.137	0.056	0.318	0.092	0.121	0.235	0.158	0.151	0.171	0.160

Table 4.4 Maximum GP K_{fs} values for upper, lower, and average of the two hillslope positions at each depth interval (cm/min).

Depth (cm)	Lower Max	Upper Max	Average Max
5-15	0.114	0.156	0.135
15-25	0.069	0.127	0.098
25-35	0.065	0.095	0.080
35-45	0.016	0.012	0.014
45-55	0.004	0.013	0.008
Berm	0.169	0.125	0.147

4.2 Micro-catchment Stage to Surface Area and Volume

The relationship between stage and surface area is presented in Figure 4.1 and the stage to volume relationship is shown in Figure 4.2. The equations relating these variables were 4th order and 2nd order polynomial expressions respectively, each with a coefficient of determination greater than 99%.

Figure 4.1 Relationship between stage in each MC to 3-D Surface Area.

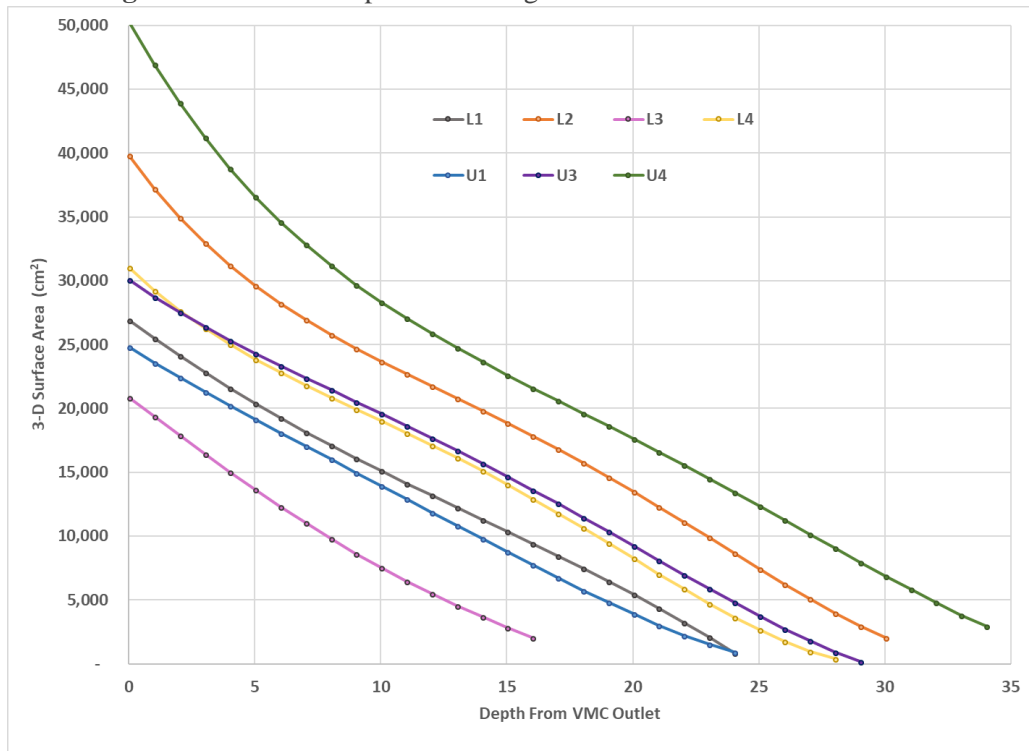
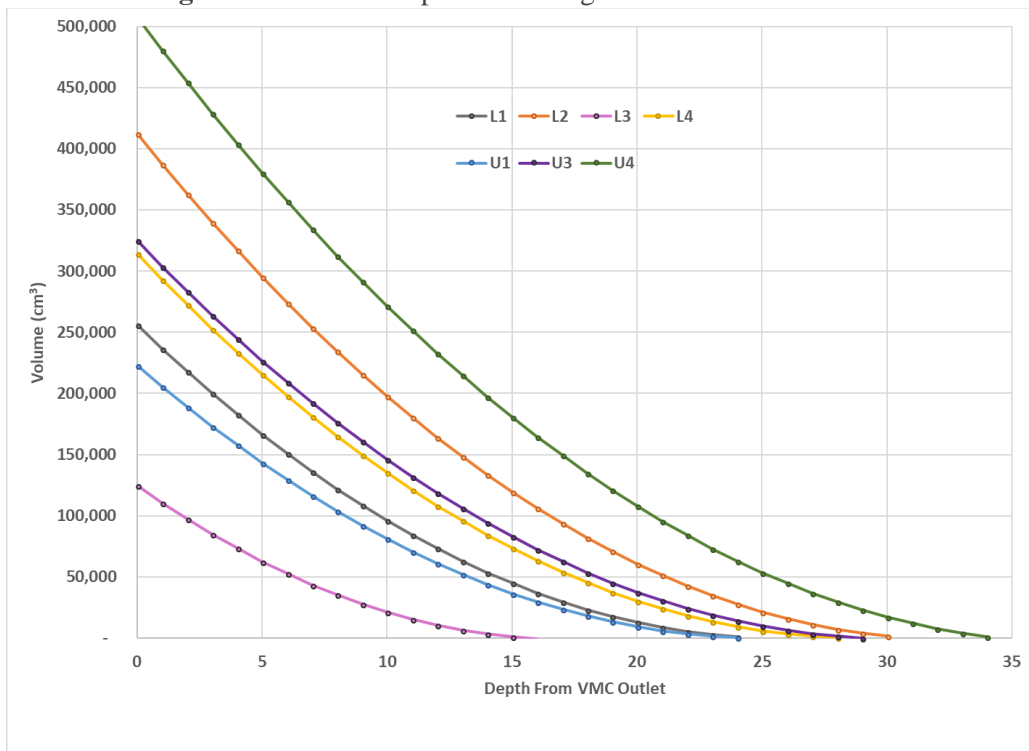


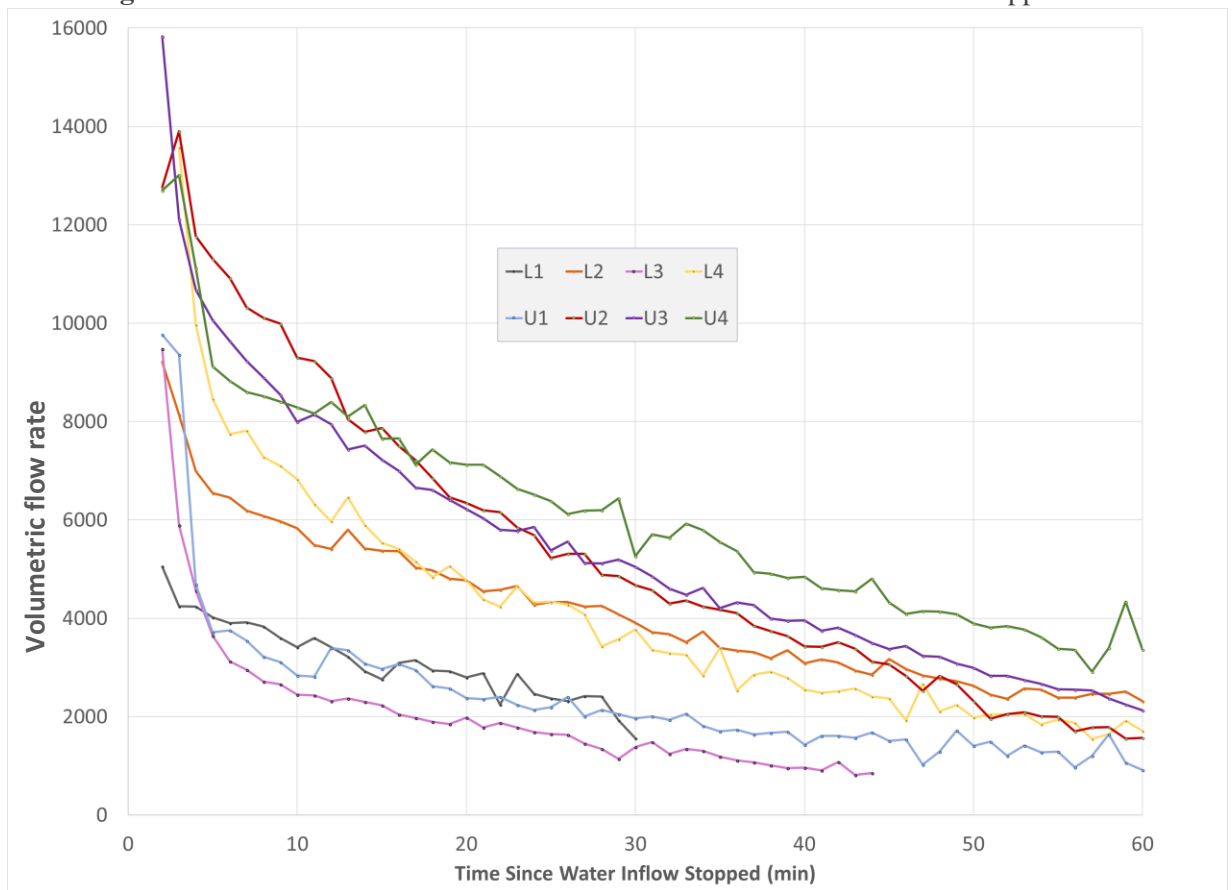
Figure 4.2 Relationship between stage in each MC to Volume.



4.3 Concentrated Flow Infiltration

When the inflow was turned off, the water began falling in each pit. This infiltration data is presented below with the volumetric flow rate infiltrating through the MC expressed as a positive volumetric flow rate. Figure 4.3 presents the data for each site. Note that U2's infiltration rates are much higher than the similarly located U1 and U3. This was due to the rodent hole that was exposed at the end of the simulation and was the reason no models were developed for U2.

Figure 4.3 Volumetric flow rate for the 60 minutes after water inflow was stopped.



4.3.1 Hydrus Model Outputs

Each Hydrus model took approximately 25-40 seconds to run. The final water balance errors ranged from 0.014 % to 0.031 %. The water balance error is a description of model uncertainty but does not reflect a comparison between measured and modeled data. The three primary ways to view the results of the model at any given timestep are pressure head, water content, and velocity. The following outputs are 2-D examples of each of these results for a typical simulation of the L1 MC at 255 minutes. At this period, there is no inflow into the MC and the water level is falling. The pressure head distribution is displayed in Figure 4.4, where the water level in the catchment is the “0” pressure head mark between the black and blue classifications. Note that this fully saturated bulb extends approximately 20 cm beneath the bottom surface of the catchment. This can also be seen in the volumetric water content (θ) distribution in Figure 4.5. Note that the color scale is the same as pressure head, but the the [-] in the legend refers to θ .

Figure 4.4 Pressure Head distribution for L1 at 255 minutes.

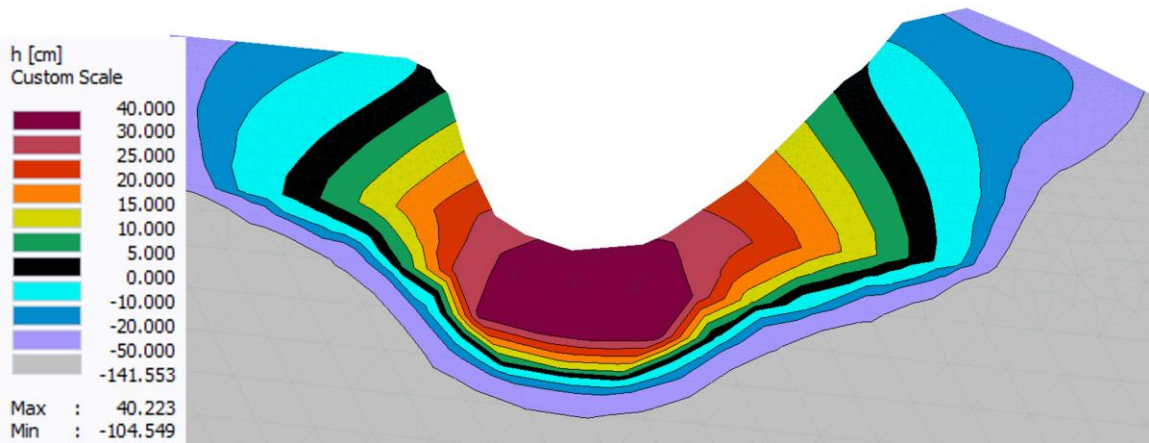
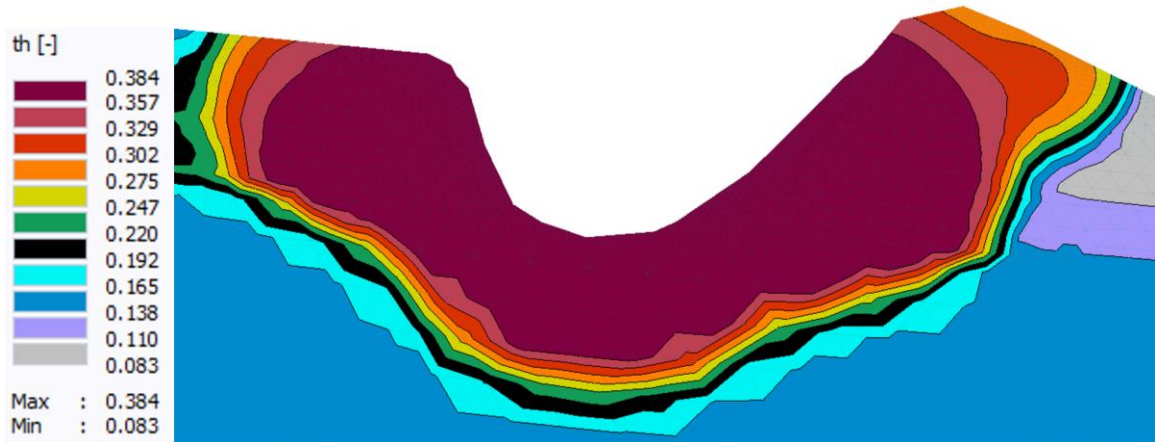


Figure 4.5 Water Content distribution for L1 at 255 minutes.



Hydrus solved the Richards equation over each finite mesh element for a known pressure head and water content, resulting in a flux of water across the FE mesh. The known pressure head distribution with a time-variable head boundary allows for calculation of flux for all areas where the water is ponded. The resulting velocity vectors are displayed in Figure 4.6. This same data can be displayed as a distribution of velocity across the model domain (Fig. 4.7). This velocity output across the boundary of the MC was used to calculate a 3-D volumetric flow rate into the subsurface. It is important to note that the model is developed in 2-D, but the flow out of each MC is in 3-D. To translate the 2-D velocity to a 3-D shape, the average velocity profile was necessary. This velocity profile can be multiplied by the surface area (Fig. 4.1) across small intervals in each MC to yield a volumetric flow rate.

Figure 4.6 Velocity vectors for L1 at 255 minutes.

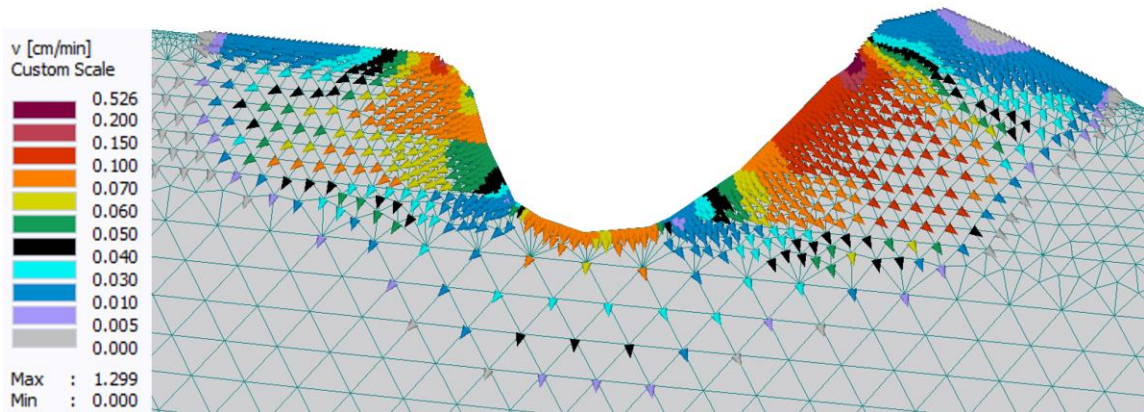
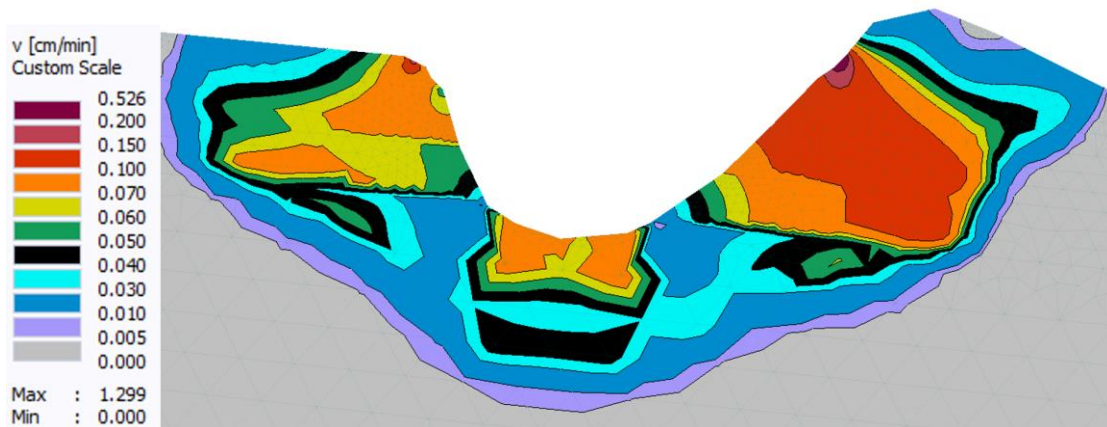


Figure 4.7 Velocity distribution for L1 at 255 minutes.



4.4 Velocity Profile Conversion to Volumetric Flow Rate

Modeled fluxes were compared to measured infiltration rates for six timesteps after the inflow into the MC ceased. Each subsequent timestep was at a 5-minute interval for a total of 30 minutes.

4.4.1 Velocity Profile

Hydrus stores information about fluxes across each boundary at each of the timesteps specified in the model. This information is output after each model run in the “boundary.out” file located within the project folder. The data for the six timesteps after the inflow was turned off were copied into Excel. The Hydrus output separates the data by each boundary type, and further divides the atmospheric boundary into a pressure head boundary (h is positive i.e., ponded water) and negative pressure head (h is negative, atmospheric boundary persists). The data of interest is the flux across the boundary where water is ponded, making it necessary to pull out the data for the positive pressure head boundary. Each output of a FE element along the boundary is associated with a x/z location within the model domain, making it possible to calculate the height within the MC. The velocity for each vertical 1 cm interval were then averaged. An example of the final output velocity profile for U4 is displayed in Table 4.5, and detailed examples for each MC are attached in the appendices. Note that as the water falls within the MC, the velocity profile does not extend to the full height of the MC.

Table 4.5 Velocity Profile for U4 (Full Results Displayed in Appendices).

Interval	Depth From top (cm)	Height Poned (cm)	SA-3D (cm ²)	SA Δ (cm ²)	Velocity (T=250)	Velocity (T=255)	Velocity (T=260)	Velocity (T=265)	Velocity (T=270)	Velocity (T=275)
U4-0	0	40.5	50,299	-						
U4-1	1	39.5	46,968	3,332	0.368					
U4-2	2	38.5	43,966	3,002	0.142	0.435				
U4-3	3	37.5	41,263	2,703	0.166	0.216				
U4-4	4	36.5	38,828	2,435	0.168	0.197	0.409			
U4-5	5	35.5	36,632	2,195	0.142	0.159	0.19	0.32		
U4-6	6	34.5	34,649	1,983	0.131	0.139	0.147	0.171		
U4-7	7	33.5	32,854	1,796	0.136	0.16	0.168	0.177	0.388	
U4-8	8	32.5	31,221	1,633	0.19	0.199	0.2	0.206	0.271	0.537
U4-9	9	31.5	29,728	1,492	0.19	0.211	0.211	0.209	0.241	0.31
U4-10	10	30.5	28,355	1,373	0.195	0.213	0.211	0.206	0.225	0.253
U4-32	32	8.5	4,822	1,020	0.088	0.083	0.077	0.073	0.069	0.067
U4-33	33	7.5	3,853	969	0.082	0.077	0.072	0.067	0.064	0.062
U4-34	34	6.5	2,951	902	0.082	0.077	0.072	0.067	0.064	0.062

4.4.2 Volumetric Flow Rate Calculation

The calculation of volumetric flow rate for each 1 cm interval is a simple multiplication of the velocity (cm/min) at a depth interval by the corresponding 3-D surface area (cm²), yielding a volumetric flow rate (cm³/min) for a 1 cm interval. The volumetric flow rate for each 1 cm interval are then summed to yield the total volumetric flow rate for a given timestep. This was calculated for each of the six intervals in each MC with a set of conductivity data described in Section 3.7.5.

4.5 Modeled and Measured Results Comparison

The modeled volumetric flow rates were compared to the field measured volumetric flow rates that were calculated in Section 4.3 and displayed in Figure 4.3. Each of the four sets of conductivity data described in Section 3.7.4 were used to run the model and yield a separate prediction. Tables 4.6 to 4.9 display results for K_s Profiles 1-4 and are all described as volumetric flow rate (cm³/min). The blue bars represent a model underprediction of flowrate, and the red indicates that the model overpredicted the flow rate. When Q_{modeled} is greater than Q_{observed} ,

negative values are indicated in parenthesis. Over the 6 periods of the simulation for each site and K_s profile, most models predicted volumetric flow rates with a similar size of error $[(\text{observed} - \text{modeled})/\text{observed}]$. This suggests that the models capture the general variation of fluxes within MCs over the 30-minute model period. However, the magnitude of error changed between sites, and with different K_s profile data. The average error at each site with each K_s profile are displayed in Table 4.10.

Table 4.6 Measured vs. modeled volumetric flow rates with K_s Profile 1

K _s Profile	Site	Timestep	Q SUM Modeled (cm ³ /min)	Q Obs (cm ³ /min)	Q Difference (obs-model) (cm ³ /min)	% Error
1	L1	T=265	3,484	4,234	750	18
1	L1	T=270	2,978	3,599	621	17
1	L1	T=275	2,738	2,923	185	6
1	L1	T=280	2,453	2,921	468	16
1	L1	T=285	2,168	2,463	295	12
1	L1	T=290	2,172	1,926	(246)	-13
1	L2	T=275	3,501	6,993	3,492	50
1	L2	T=280	2,185	5,973	3,788	63
1	L2	T=285	2,090	5,418	3,328	61
1	L2	T=290	2,189	4,806	2,617	54
1	L2	T=295	1,992	4,273	2,281	53
1	L2	T=300	1,946	4,080	2,134	52
1	L3	T=235	2,102	2,855	753	26
1	L3	T=240	1,858	2,218	360	16
1	L3	T=245	1,536	1,865	329	18
1	L3	T=250	1,345	1,624	279	17
1	L3	T=255	1,121	1,482	361	24
1	L4	T=230	3,902	7,748	3,846	50
1	L4	T=235	3,094	6,321	3,227	51
1	L4	T=240	2,404	5,412	3,008	56
1	L4	T=245	2,114	4,386	2,272	52
1	L4	T=250	1,740	4,280	2,540	59
1	L4	T=255	1,555	3,359	1,804	54
1	U1	T=240	7,786	3,543	(4,243)	-120
1	U1	T=245	6,427	3,396	(3,031)	-89
1	U1	T=250	5,880	2,945	(2,935)	-100
1	U1	T=255	5,035	2,400	(2,635)	-110
1	U1	T=260	5,206	2,002	(3,204)	-160
1	U1	T=265	3,995	1,936	(2,059)	-106
1	U3	T=250	7,708	3,543	(4,165)	-118
1	U3	T=255	7,402	3,396	(4,006)	-118
1	U3	T=260	6,057	2,945	(3,112)	-106
1	U3	T=265	5,072	2,400	(2,672)	-111
1	U3	T=270	4,033	2,002	(2,031)	-101
1	U3	T=275	3,268	1,936	(1,332)	-69
1	U4	T=250	9,744	11,117	1,373	12
1	U4	T=255	10,767	8,402	(2,365)	-28
1	U4	T=260	9,078	8,334	(744)	-9
1	U4	T=265	8,008	7,173	(835)	-12
1	U4	T=270	7,328	6,514	(814)	-12
1	U4	T=275	7,128	6,438	(690)	-11

Table 4.7 Measured vs. modeled volumetric flow rate with K_s Profile 2.

K _s Profile	Site	Timestep	Q SUM Modeled (cm ³ /min)	Q Obs (cm ³ /min)	Q Difference (obs-model) (cm ³ /min)	% Error
2	L1	T=265	2,586	4,234	1,648	39
2	L1	T=270	2,149	3,599	1,450	40
2	L1	T=275	1,963	2,923	960	33
2	L1	T=280	1,716	2,921	1,205	41
2	L1	T=285	1,502	2,463	961	39
2	L1	T=290	1,498	1,926	428	22
2	L2	T=275	2,269	6,993	4,724	68
2	L2	T=280	1,140	5,973	4,833	81
2	L2	T=285	1,093	5,418	4,325	80
2	L2	T=290	1,163	4,806	3,643	76
2	L2	T=295	1,010	4,273	3,263	76
2	L2	T=300	994	4,080	3,086	76
2	L3	T=235	1,078	2,855	1,777	62
2	L3	T=240	945	2,218	1,273	57
2	L3	T=245	790	1,865	1,075	58
2	L3	T=250	702	1,624	922	57
2	L3	T=255	593	1,482	889	60
2	L4	T=230	2,722	7,748	5,026	65
2	L4	T=235	2,049	6,321	4,272	68
2	L4	T=240	1,503	5,412	3,909	72
2	L4	T=245	1,221	4,386	3,165	72
2	L4	T=250	967	4,280	3,313	77
2	L4	T=255	846	3,359	2,513	75
2	U1	T=240	4,608	3,543	(1,065)	-30
2	U1	T=245	3,707	3,396	(311)	-9
2	U1	T=250	3,348	2,945	(403)	-14
2	U1	T=255	2,820	2,400	(420)	-18
2	U1	T=260	2,867	2,002	(865)	-43
2	U1	T=265	2,211	1,936	(275)	-14
2	U3	T=250	5,322	3,543	(1,779)	-50
2	U3	T=255	5,117	3,396	(1,721)	-51
2	U3	T=260	4,131	2,945	(1,186)	-40
2	U3	T=265	3,368	2,400	(968)	-40
2	U3	T=270	2,690	2,002	(688)	-34
2	U3	T=275	2,197	1,936	(261)	-13
2	U4	T=250	7,478	11,117	3,639	33
2	U4	T=255	8,291	8,402	111	1

Table 4.8 Measured vs. modeled volumetric flow rate with K_s Profile 3.

K _s Profile	Site	Timestep	Q SUM Modeled (cm ³ /min)	Q Obs (cm ³ /min)	Q Difference (obs-model) (cm ³ /min)	% Error
3	L1	T=265	2,093	4,234	2,141	51
3	L1	T=270	1,662	3,599	1,937	54
3	L1	T=275	1,490	2,923	1,433	49
3	L1	T=280	1,243	2,921	1,678	57
3	L1	T=285	1,028	2,463	1,435	58
3	L1	T=290	1,027	1,926	899	47
3	L2	T=275	1,426	6,993	5,567	80
3	L2	T=280	1,201	5,973	4,772	80
3	L2	T=285	942	5,418	4,476	83
3	L2	T=290	1,010	4,806	3,796	79
3	L2	T=295	925	4,273	3,348	78
3	L2	T=300	759	4,080	3,321	81
3	L3	T=235	851	2,855	2,004	70
3	L3	T=240	713	2,218	1,505	68
3	L3	T=245	555	1,865	1,310	70
3	L3	T=250	464	1,624	1,160	71
3	L3	T=255	359	1,482	1,123	76
3	L4	T=230	1,981	7,748	5,767	74
3	L4	T=235	1,706	6,321	4,615	73
3	L4	T=240	1,142	5,412	4,270	79
3	L4	T=245	886	4,386	3,500	80
3	L4	T=250	639	4,280	3,641	85
3	L4	T=255	509	3,359	2,850	85
3	U1	T=240	3,810	3,543	(267)	-8
3	U1	T=245	3,016	3,396	380	11
3	U1	T=250	2,687	2,945	258	9
3	U1	T=255	2,184	2,400	216	9
3	U1	T=260	2,242	2,002	(240)	-12
3	U1	T=265	1,627	1,936	309	16
3	U3	T=250	3,333	3,543	210	6
3	U3	T=255	3,216	3,396	180	5
3	U3	T=260	2,366	2,945	579	20
3	U3	T=265	1,738	2,400	662	28
3	U3	T=270	1,201	2,002	801	40
3	U3	T=275	838	1,936	1,098	57
3	U4	T=250	5,494	11,117	5,623	51
3	U4	T=255	6,261	8,402	2,141	25
3	U4	T=260	4,794	8,334	3,540	42
3	U4	T=265	3,974	7,173	3,199	45
3	U4	T=270	3,451	6,514	3,063	47
3	U4	T=275	3,300	6,438	3,138	49

Table 4.9 Measured vs. modeled volumetric flow rate with K_s Profile 4

K _s Profile	Site	Timestep	Q SUM Modeled (cm ³ /min)	Q Obs (cm ³ /min)	Q Difference (obs-model) (cm ³ /min)	% Error
4	L1	T=265	3,928	4,234	306	7
4	L1	T=270	3,318	3,599	281	8
4	L1	T=275	3,002	2,923	(79)	-3
4	L1	T=280	2,647	2,921	274	9
4	L1	T=285	2,290	2,463	173	7
4	L1	T=290	2,279	1,926	(353)	-18
4	L2	T=275	2,777	6,993	4,216	60
4	L2	T=280	2,440	5,973	3,533	59
4	L2	T=285	2,054	5,418	3,364	62
4	L2	T=290	2,231	4,806	2,575	54
4	L2	T=295	2,136	4,273	2,137	50
4	L2	T=300	1,866	4,080	2,214	54
4	L3	T=235	2,869	2,855	(14)	0
4	L3	T=240	2,552	2,218	(334)	-15
4	L3	T=245	2,052	1,865	(187)	-10
4	L3	T=250	1,786	1,624	(162)	-10
4	L3	T=255	1,432	1,482	50	3
4	L4	T=230	4,530	7,748	3,218	42
4	L4	T=235	3,990	6,321	2,331	37
4	L4	T=240	3,038	5,412	2,374	44
4	L4	T=245	2,701	4,386	1,685	38
4	L4	T=250	2,111	4,280	2,169	51
4	L4	T=255	1,902	3,359	1,457	43
4	U1	T=240	4,985	3,543	(1,442)	-41
4	U1	T=245	4,013	3,396	(617)	-18
4	U1	T=250	3,594	2,945	(649)	-22
4	U1	T=255	2,970	2,400	(570)	-24
4	U1	T=260	3,101	2,002	(1,099)	-55
4	U1	T=265	2,236	1,936	(300)	-16
4	U3	T=250	4,680	3,543	(1,137)	-32
4	U3	T=255	4,463	3,396	(1,067)	-31
4	U3	T=260	3,482	2,945	(537)	-18
4	U3	T=265	2,767	2,400	(367)	-15
4	U3	T=270	2,070	2,002	(68)	-3
4	U3	T=275	1,570	1,936	366	19
4	U4	T=250	6,426	11,117	4,691	42
4	U4	T=255	7,056	8,402	1,346	16
4	U4	T=260	5,628	8,334	2,706	32
4	U4	T=265	4,826	7,173	2,347	33
4	U4	T=270	4,274	6,514	2,240	34
4	U4	T=275	4,088	6,438	2,350	36

Table 4.10 Measured vs. Modeled average values comparison by site for all K_s Profiles

K_s Profile	Site	Q SUM Modeled (cm ³ /min)	Q Obs (cm ³ /min)	Q Difference (obs-model) (cm ³ /min)	% Error
1	L1	2666	3011	345	9
	L2	2317	5257	2940	56
	L3	1592	2009	416	20
	L4	2468	5251	2783	54
	U1	5722	2704	-3018	-114
	U3	5590	2704	-2886	-104
	U4	8676	7996	-679	-10
	1 avg	4210	4185	-25	-13
2	L1	1902	3011	1109	36
	L2	1278	5257	3979	76
	L3	822	2009	1187	59
	L4	1551	5251	3700	72
	U1	3260	2704	-557	-21
	U3	3804	2704	-1100	-38
	U4	6388	7996	1608	20
	2 avg	2761	4185	1424	28
3	L1	1424	3011	1587	53
	L2	1044	5257	4213	80
	L3	589	2009	1420	71
	L4	1144	5251	4107	79
	U1	2594	2704	109	4
	U3	2115	2704	588	26
	U4	4546	7996	3451	43
	3 avg	1955	4185	2230	50
4	L1	2911	3011	100	2
	L2	2251	5257	3006	57
	L3	2138	2009	-130	-6
	L4	3045	5251	2206	42
	U1	3483	2704	-780	-29
	U3	3172	2704	-469	-14
	U4	5383	7996	2613	32
	4 avg	3223	4185	961	12
all	all avg	3037	4185	1148	19

4.6 2-D vs. Axisymmetric Results

The difference between the original (2-D vertical) and the axisymmetric model are shown below using the hydraulic parameters and boundary data from L1. The axisymmetric model had on

average 11% greater velocity across the boundary, resulting in a change of 8% in volumetric flow rate for L1 (Table 4.11).

Table 4.11 Change in velocity and volumetric flow rate model results (original – axisymmetric).

Timestep (min)	Velocity (q) (% difference)	Volumetric flow rate (Q) (% difference)
265	-9%	6%
270	-9%	7%
275	-11%	9%
280	-11%	8%
285	-11%	8%
290	-13%	12%
Average	-11%	8%

5 Discussion

The change in error measured over each interval for the 30-minute period is an indication of how well the infiltration dynamics were captured for each site. Over this period, the measured volumetric flow rate would usually drop by about half as the water level in MCs dropped between 4 to 10 cm. While the drop-in water level was not necessarily large compared to the total MC depth, this often corresponded to the water level dropping below the higher conductivity soils of the berm and uppermost layer of soil. An order of magnitude reduction in K_s measured by the GP was not uncommon between the berm and lower soil layers. If the model is doing a poor job capturing the infiltration dynamics, we would expect the error to change with each observation time-step. For most modeled sites, the error between modeled and measured results was similar over each timestep, so the model performed in a consistent manner despite changing proportions of K_s values. Some sites, such as U3, had substantial variation using all K_s models. This indicates that either none of the K_s profiles tests were a good representation of U3, or the site had additional complexity that we did not identify in the model. Most sites and K_s profiles did appear to capture the infiltration behavior within a MC. However, the magnitude of predicted volumetric flow rates was highly dependent on the input K_s values.

5.1 K_s Profile 1

Using the K_s Profile 1 (PSD data only) the lower sites underpredicted volumetric flow rates by 35%, while the upper sites were overpredicted by 76%. The average error for K_s Profile 1 was only off by 13%, yet the absolute error was 54%. There are many explanations for the inaccuracy of these results. The dataset that was used was to generate the conductivity values relied on pedotransfer functions and were not direct measurements of K_s . These measurements would not

pick up on something such as silica build up in the soil profile that would reduce the conductivity. It is preferable to directly measure K_s using a GP, or another direct measurement such as a double ring infiltrometer. Despite the limitations of K_s Profile 1, Site L1, L3 and U4 were on average within 20% of most observations. Sites U1 and U3 overpredicted by over 100%.

One important note is that the PSD was an average of two measurements for the upper and two measurements for the lower sites. The upper sites overpredicted flow rates while the lower sites underpredicted flow rates. Separating upper and lower sites may have done worse than assuming a similar conductivity profile for the two hillslope positions. An average of all four sample locations at upper and lower sites would have allowed some of the observed error to cancel out, providing a more accurate result than separating K_s input data by hillslope position. Additional soil samples would need to be taken to determine if the variability between upper and lower sites was an indication of physical differences between sites, or just a result of under-sampling.

5.2 K_s Profile 2

K_s Profile 2 acknowledged that there was some uncertainty about how well the GP measured flow in the lower conductivity soils that were greater than 35 cm of depth. Many of the measurements greater than 35 were under 0.008 cm/min and almost completely restricted flow into the lower profile. Those flow rates are near the lower threshold that the GP could measure and were replaced by PSD data. Using the K_s Profile 2 (GP 2018 for <35 cm, PSD data for >35), the lower sites all underpredicted volumetric flow rate by an average of 61%, while the upper sites were on average within 13% of observed values. Despite the relatively small error at the upper sites, this situation may be somewhat coincidental because the profile of K_s was quite unrealistic for the upper site. The upper site K_s values between 25-35 cm from the GP were much lower than the K_s values given by the PSD data greater than 35 cm; this inversion was not observed in the field.

Since the K_s limiting layer (25-35 cm) was submerged over the entire simulation, this unrealistic scenario did not result in significant change in error over the 30-minute observation period. The K_s Profile 2 results suggest that combining K_s measurements made with different methodologies in a single profile can result in unrealistic physical models of MC infiltration, even if model predictions are relatively accurate.

5.3 K_s Profile 3

When the model is parameterized by K_s Profile 3 (GP 2018 data only), the lower sites underpredicted by an average of 71%, while the upper sites were on average 24% lower than observed data. The severe underprediction of volumetric flow rate can be attributed to three reasons:

1. Uniform flow models do not consider the more complex structure within the soil. While many of the deeper layers had low conductivity values, preferential pathways are observed in almost all soils [*Germain and Hensel, 2006*]. Fractures in the soil profile or structured soil can provide pathways for water to move more rapidly than would be predicted by the Richards Equation.
2. The scale of GP measurements is not representative of a MC. Over one-hundred GP measurements would not cover the surface area of any single MC. In the much larger MC, water will flow along preferential flow paths that would not necessarily be sampled by the narrow well of GP measurements.
3. The model is not fully considering 3-D flow (Section 4.6). Results comparing 2-D vertical to 2-D axisymmetric indicated an average increase of velocity by 11%, resulting in 8% larger volumetric flow rate.

The difference between upper and lower sites is likely related to the first two reasons provided above. The higher flow rates relative to measured conductivity values in the lower sites could indicate more preferential pathways for the water to flow through. One cause for this disparity could be the difference in biological activity in the upper and lower sites. The plants in the lower site may have had a deeper rooting depth, creating flowpaths at greater depth within the soil. Rodent holes and ant hills were frequent within the study area. Even if a MC did not directly intersect any subsurface animal holes, the water could have been accessing these larger flow paths as it moved into the subsurface.

5.4 K_s Profile 4

K_s Profile 4 (Max GP values averaged separately for upper and lower) was intended to acknowledge that flow out of a large MC may be concentrated along paths of high conductivity and that small GP wells might not capture such examples of preferential flow, so the maximum estimated K_s from GP measurements might be best. The Hydrus model with K_s Profile 4 underpredicted by 24% for lower sites and was within an average of 1% for the upper sites. Of the four K_s models, K_s Profile 4 made the most accurate predictions of flow with an average error of 12%. The use of maximum GP measurements likely provided a better model of preferential flow that was applicable to the scale of MCs. The average underprediction by 12% could reasonably be explained by differences in 2-D and 3-D flow (Table 4.12). The exact number of measurements required to make a representative K_s profile is not well constrained. A different soil may require more or fewer samples to represent the spatial heterogeneity. Future research should take into consideration the importance of sample size and preferential flow in predicting infiltration rates into micro-catchments.

5.5 Improvements and Next Steps

This research effort predicted infiltration in MCs based on 2-D Hydrus simulations for a single event. Future work could adapt simulations to more complex scenarios to answer pertinent research questions, such as representing weather patterns over a seasonal time scale. This would have the advantage of developing a flow budget for the MCs, including quantification of total water stored in the soil profile. A water budget would also allow for Hydrus simulation of plant growth within MCs. The Hydrus model could also be used in conjunction with other physically based models such as RHEM. RHEM could solve for erosion and flow rates entering a catchment from upslope, and Hydrus could determine whether infiltration capacity of a MC would likely be exceeded. This would allow land managers to test potential configurations of MCs at the hillslope scale, that have minimal risk of increasing erosion.

One important question for future research is what measurements can be made to quickly and accurately represent a new field site? The GP was effective at rapidly collecting data across a soil profile. A single person was able to carry out 58 measurements in two field days. This was ideal to determine that there were flow limiting layers at depth in almost all sites. However, the small spatial scale of the measurements may miss larger scale flow processes taking place in the soil. An instrument such as a double ring infiltrometer might do a better job predicting flow rates due to larger observational surface area. However, most often double ring infiltrometers are only used for the surface layer of soil. Overall, the GP was an effective instrument to rapidly characterize K_s with depth. The GP is recommended for future use to survey sites, but the issues of small observational scale relative to MCs does need to be considered. Future research efforts may benefit from increasing the number of GP measurements to better characterize spatial variability in K_s at a field site being considered for restoration.

Another simple way to improve soil measurements would be to carry out a laboratory analysis of soils to determine hydraulic parameters using inverse Hydrus solutions. While this would greatly improve some estimates, it would be difficult to representatively sample a heterogeneous soil. There is also error related to use of a uniform flow model. While use of a dual permeability model may be the most physically realistic, a much larger effort would be necessary to determine hydraulic parameters related to non-uniform flow [Simunek *et al.*, 2003]. Predicting infiltration into soils is a very complex process dependent on accurate understanding of soil hydraulic parameters. Future research will need to further develop what is an acceptable level of effort to characterize a field site so that infiltration can be predicted.

The process developed in this paper is applicable far beyond infiltration into MCs. A 2-D representation of a MC was used in a Hydrus model to output a 1-D velocity profile. The profile could be multiplied by surface area over any interval to predict a volumetric flow rate into the subsurface. This concept could be applied to a much larger scale. All that is required is an accurate DEM to understand how surface area changes with stage. The author of this paper is not aware of any literature involving Hydrus where this type of approach has been previously applied. Infiltration could be predicted for a large system such as a field or wetland, where a 3D Hydrus model would be computationally prohibitive. This would allow resource managers to apply a physically based model to solve for infiltration in the place of simplified analytical expressions that are frequently used.

6 Conclusion

Infiltration experiments were carried out on eight MCs. The infiltration rate within each pit was observed using stage measurements and geometric relationships developed from 3-D models of each MC. Soil measurements with a GP were taken to a maximum depth of 55 cm to predict volumetric flow rates observed in each MC. A 2-D Hydrus model was developed to represent MC function and initial conditions were set to mimic field experiments. The model output for velocity of water across the model boundary was converted into a velocity profile. This velocity profile was multiplied by the corresponding surface area and summed to yield a volumetric flow rate at any given timestep. Flow rates predicted at six intervals were output from the model for 30 minutes after the inflow to each MC was stopped. Each of those values were compared to observed data for the respective MC and timestep using model outputs parameterized with four sets of K_s data. The variation in error over each time interval for most sites indicated that general infiltration dynamics were captured as the water level dropped to lower layers in the soil profile. However, the magnitude of predicted infiltration was highly dependent on the input K_s . Many sites were severely underpredicted fluxes. Sources of error likely resulted from preferential flow paths not represented in the model, differences in scale between the permeameter wells and the MCs, and the difference between 2-D and 3-D flow. K_s Profile 4, where the maximum GP K_s data at each depth was averaged separately for upper and lower sites, was the best representation of the flow processes taking place within a MC with an average underprediction of 12%. The method of using Hydrus to yield a velocity profile was an effective way to predict infiltration into the unsaturated zone. Further work could improve methods to measure soil hydraulic properties and may consider incorporation of a non-uniform flow model. The models presented in this paper should be considered for adaptation to answer more complex questions about micro-catchment ponded infiltration occurring over larger spatial and temporal domains.

The modeling process was developed to evaluate the efficacy of hillslope restoration using the Vallerani system. The model currently provides volumetric flow rates at each level of ponded water within a MC. The volumetric flow rate observed at the initial time interval after the inflow stopped is the maximum infiltration capacity of a MC. While predicting the maximum volumetric flow rate out of a MC is very useful, the incoming discharge into the MC from upslope has not been fully integrated with this effort. Event-based flow and erosion models such as RHEM could be used to create a time series of incoming discharge into a MC based on the upslope conditions which could be applied in Hydrus to determine infiltration dynamics. This step would make the model useful as a planning tool to determine whether a configuration of MCs on a hillslope are adequately spaced to infiltrate runoff from a storm event. From an erosion management perspective, this is a critical step in designing a successful restoration strategy. Furthermore, the positive impacts of a mitigation strategy could be quantitatively compared across sites, or to other restoration strategies.

7 Literature Cited

- Akbar, G., S. Raine, A. D. McHugh, and G. Hamilton (2015), Managing lateral infiltration on wide beds in clay and sandy clay loam using Hydrus 2D, *Irrigation Science*, 33(3), 177-190.
- Ali, S., A. Islam, P. K. Mishra, and A. K. Sikka (2016), Green-Ampt approximations: A comprehensive analysis, *Journal of Hydrology*, 535, 340-355.
- Aravena, J. E., and A. Dussailant (2009), Storm-Water Infiltration and Focused Recharge Modeling with Finite-Volume Two-Dimensional Richards Equation: Application to an Experimental Rain Garden, *Journal of Hydraulic Engineering-Asce*, 135(12), 1073-1080.
- Assouline, S., and Y. Mualem (2002), Infiltration during soil sealing: The effect of areal heterogeneity of soil hydraulic properties, *Water Resources Research*, 38(12).
- Bautista, E., A. W. Warrick, J. L. Schlegel, K. R. Thorp, and D. J. Hunsaker (2016), Approximate Furrow Infiltration Model for Time-Variable Ponding Depth, *Journal of Irrigation and Drainage Engineering*, 142(11), 11.
- Blank, R. (2018), personal interview with M. Founds.
- Bouwer, H. (2002), Artificial recharge of groundwater: hydrogeology and engineering, *Hydrogeology Journal*, 10(1), 121-142.
- Breshears, D. D., J. J. Whicker, M. P. Johansen, and J. E. Pinder (2003), Wind and water erosion and transport in semi-arid shrubland, grassland and forest ecosystems: Quantifying dominance of horizontal wind-driven transport, *Earth Surface Processes and Landforms*, 28(11), 1189-1209.
- Broadbridge, P., and I. White (1988), Constant rate rainfall infiltration - A Versatile nonlinear model .I. analytic solution, *Water Resources Research*, 24(12), 2109-2110.
- Buckingham, E. (1907), Studies on the movement of soil moisture, Bull. 38, Bur. of Soils, USDA, Washington, D. C.
- Bureau of Reclamation (2013), Quality of Water Colorado River Basin Progress Report No. 24Rep. U.S. Department of Interior.
- Bureau of Reclamation (2017), Quality of Water Colorado River Basin Progress Report No. 25Rep., U.S. Department of Interior.
- Darcy, H. (1856), Détermination des lois d'écoulement de l'eau à travers le sable, Les Fontaines Publiques de la Ville de Dijon, pp. 590-594, Victor Dalmont, Paris.
- Ebrahimian, H., A. Liaghat, M. Parsinejad, F. Abbasi, and M. Navabian (2012), Comparison of One- and Two-Dimensional Models to Simulate Alternate and Conventional Furrow Fertilization, *Journal of Irrigation and Drainage Engineering*, 138(10), 929-938.
- Elrick, D. E., W. D. Reynolds, and K. A. Tan (1989), Hydraulic conductivity measurements in the unsaturated zone using improved well analyses, *Ground Water Monitoring and Remediation*, 9(3), 184-193.
- Finch, S. D., D. E. Radcliffe, and L. T. West (2008), Modeling trench sidewall and bottom flow in on-site wastewater systems, *Journal of Hydrologic Engineering*, 13(8), 693-701.
- Gardner, W. R. (1958), Some steady state solutions of the unsaturated moisture flow equation with application to evaporation from a water table, *Soil Sci.*, 85, 228-232.
- Germann, P. F., and D. Hensel (2006), Poiseuille flow geometry inferred from velocities of wetting fronts in soils, *Vadose Zone Journal*, 5(3), 867-876.
- Goodrich, D. C., J. M. Faures, D. A. Woolhiser, L. J. Lane, and S. Sorooshian (1995), Measurement and analysis of small-scale convective storm rainfall variability, *Journal of Hydrology*, 173(1-4), 283-308.

- Green, W. H., and G. A. Ampt (1911), Studies on soils physics: 1. The flow of air and water through soils, *J. Agric. Sci.*, 4, 1–24.
- Hayek, M. (2014), Water pulse migration through semi-infinite vertical unsaturated porous column with special relative-permeability functions: Exact solutions, *Journal of Hydrology*, 517, 668-676.
- Hayek, M. (2016), Analytical solution to transient Richards' equation with realistic water profiles for vertical infiltration and parameter estimation, *Water Resources Research*, 52(6), 4438-4457.
- Heilweil, V. M., J. Benoit, and R. W. Healy (2015), Variably saturated groundwater modelling for optimizing managed aquifer recharge using trench infiltration, *Hydrological Processes*, 29(13), 3010-3019.
- Hernandez, M., Nearing, M. A., Al-Hamdan, O. Z., Pierson, F. B., Armendariz, G., Weltz, M. A., ... Holifield Collins, C. D. (2017). The rangeland hydrology and erosion model: A dynamic approach for predicting soil loss on rangelands. *Water Resources Research*, 53, 9368–9391. <https://doi.org/10.1002/2017WR020651>
- Malagnoux, M. (2008), Degraded Arid Land Restoration for Afforestation and Agro-Silvo-Pastoral Production through New Water Harvesting Mechanized Technology, *Future of Drylands*, 269-282.
- Maurer, D. K., D. L. Berger, M. L. Tumbusch, and M. J. Johnson (2006), Rates of evapotranspiration, recharge from precipitation beneath selected areas of native vegetation, and streamflow gain and loss in Carson Valley, Douglas County, Nevada, and Alpine County, California: U.S. Geological Survey Scientific Investigations Report 2005-5288Rep., 70 p pp, U.S. Geological Survey.
- Mualem, Y. (1976), New model for predicting hydraulic conductivity of unsaturated porous-media, *Water Resources Research*, 12(3), 513-522.
- Nearing, M. A., H. Wei, J. J. Stone, F. B. Pierson, K. E. Spaeth, M. A. Weltz, D. C. Flanagan, and M. Hernandez (2011), A Rangeland Hydrology and Erosion Model, *Transactions of the Asabe*, 54(3), 901-908.
- NRCS (2003), *National Range and Pasture Handbook*, United States Department of Agriculture.
- NRCS (2017), Official Series Description - Bedell Series, in *Official Soil Series Descriptions*, edited by NRCS.
- Oweis, T. Y. (2017), Rainwater harvesting for restoring degraded dry agro-pastoral ecosystems: a conceptual review of opportunities and constraints in a changing climate, *Environmental Reviews*, 25(2), 135-162.
- Oweis, T., M. Karrou, Ziadat, Feras & Awawdeh, F. Oweis, T. Y., M. Karrou, F. Ziadat, and F. Awawdeh (2011), Rehabilitation and integrated management *Rep.*, International Center for Agricultural Research in the Dry Areas (ICARDA), Aleppo, Syria.
- Paige, G. B., J. J. Stone, J. R. Smith, and J. R. Kennedy (2004), The walnut gulch rainfall simulator: A computer-controlled variable intensity rainfall simulator, *Applied Engineering in Agriculture*, 20(1), 25-31.
- Pierson, F. B., P. R. Robichaud, C. A. Moffet, K. E. Spaeth, S. P. Hardegree, P. E. Clark, and C. J. Williams (2008), Fire effects on rangeland hydrology and erosion in a steep sagebrush-dominated landscape, *Hydrological Processes*, 22(16), 2916-2929.
- Radcliffe, D. E. a. S., J. (2010), *Soil Physics with Hydrus: Modeling and Applications*, CRC Press, Boca Raton, Florida.
- Rasely, R. C., T. C. Roberts, and G. P. Pyper (1991), Upper Colorado River Basin Rangeland Salinity
- Reynolds, W. D., and D. E. Elrick (1985), Insitu measurement of field-saturated hydraulic conductivity, sorptivity, and the alpha-parameter using the Guelph Permeameter, *Soil Science*, 140(4), 292-302.
- Reynolds, W. D., and D. E. Elrick (1986), A method for simultaneous insitu measurement in the THE vadose zone of field-saturated hydraulic conductivity, sorptivity and the conductivity-pressure head relationship, *Ground Water Monitoring and Remediation*, 6(1), 84-95.
- Richards, L. A. (1931), Capillary conduction of liquids through porous medium, *Physics*, 1, 318–333.

- Schaap, M. G., F. J. Leij, and M. T. van Genuchten (2001), ROSETTA: a computer program for estimating soil hydraulic parameters with hierarchical pedotransfer functions, *Journal of Hydrology*, 251(3-4), 163-176.
- Selker, J. S., and S. Assouline (2017), An explicit, parsimonious, and accurate estimate for ponded infiltration into soils using the Green and Ampt approach, *Water Resources Research*, 53(8), 7481-7487.
- Selker, J. S., K. Keller, and J. McCord (1999), *Vadose Zone Processes*, 339 pp., CRC Press, Boca Raton, Fla.
- Simunek, J., and M. T. van Genuchten (2008), Modeling nonequilibrium flow and transport processes using HYDRUS, *Vadose Zone Journal*, 7(2), 782-797.
- Simunek, J., and S. A. Bradford (2008), Vadose zone modeling: Introduction and importance, *Vadose Zone Journal*, 7(2), 581-586.
- Simunek, J., M. T. van Genuchten, and M. Sejna (2008), Development and applications of the Hydrus and Stanmod software packages and related codes, *Vadose Zone Journal*, 7(2), 587-600.
- Simunek, J., M. T. van Genuchten, and M. Sejna (2012), HYDRUS: Model use, calibration, and validation, *Transactions of the Asabe*, 55(4), 1261-1274.
- Simunek, J., M. Sejna, and M. T. van Genuchten (2018), New features of version 3 of the Hydrus (2D/3D) computer software package, *Journal of Hydrology and Hydromechanics*, 66(2), 133-142.
- Simunek, J., N. J. Jarvis, M. T. van Genuchten, and A. Gardenas (2003), Review and comparison of models for describing non-equilibrium and preferential flow and transport in the vadose zone, *Journal of Hydrology*, 272(1-4), 14-35.
- Siyal, A. A., K. L. Bristow, and J. Simunek (2012), Minimizing nitrogen leaching from furrow irrigation through novel fertilizer placement and soil surface management strategies, *Agricultural Water Management*, 115, 242-251.
- Spaeth, K. E., F. B. Pierson, M. A. Weltz, and J. B. Awang (1996), Gradient analysis of infiltration and environmental variables as related to rangeland vegetation, *Transactions of the Asae*, 39(1), 67-77.
- Strohmeier, S. (2017), email with M. Founds.
- van Genuchten, M. T. (1980), A closed-form equation for predicting the hydraulic conductivity of unsaturated soils, *Soil Science Society of America Journal*, 44(5), 892-898.
- Wang, J., G. H. Huang, H. B. Zhan, B. P. Mohanty, J. H. Zheng, Q. Z. Huang, and X. Xu (2014), Evaluation of soil water dynamics and crop yield under furrow irrigation with a two-dimensional flow and crop growth coupled model, *Agricultural Water Management*, 141, 10-22.
- Warrick, A. W., N. Lazarovitch, A. Furman, and D. Zerihun (2007), Explicit infiltration function for furrows, *Journal of Irrigation and Drainage Engineering*, 133(4), 307-313.
- Weaver, J. E., and W. M. Noll (1935), Measurement of Run-Off and Soil Erosion by a Single Investigator, *Ecology*, 16, 1-12.
- Weltz, M. A., et al. (2008), Assessing the benefits of grazing land conservation practices, *Journal of Soil and Water Conservation*, 63(6), 214A-217A.
- Zhang, Z. F. F., P. H. Groenevelt, and G. W. Parkin (1998), The well-shape factor for the measurement of soil hydraulic properties using the Guelph Permeameter, *Soil & Tillage Research*, 49(3), 219-221.
- Ziadat, F., A. Bruggeman, T. Oweis, N. Haddad, S. Mazahreh, W. Sartawi, and M. Syuof (2012), A Participatory GIS Approach for Assessing Land Suitability for Rainwater Harvesting in an Arid Rangeland Environment, *Arid Land Research and Management*, 26(4), 297-311.

8 Appendices

Appendix 1. L1 output for velocity and volumetric flow rate with K dataset 4

Height Interval	Depth From top (cm)	SA-3D (cm ²)	SA-Change (cm ²)	Velocity (T=265) (cm/min)	Velocity (T=270) (cm/min)	Velocity (T=275) (cm/min)	Velocity (T=280) (cm/min)	Velocity (T=285) (cm/min)	Velocity (T=290) (cm/min)	Q int (T=265) (cm ³ /min)	Q int (T=270) (cm ³ /min)	Q int (T=275) (cm ³ /min)	Q int (T=280) (cm ³ /min)	Q int (T=285) (cm ³ /min)	Q int (T=290) (cm ³ /min)
L1-0	0	26,945	-							-	-	-	-	-	-
L1-1	1	25,500	1,445	0.365						528	-	-	-	-	-
L1-2	2	24,129	1,371	0.240	0.302					329	413	-	-	-	-
L1-3	3	22,827	1,303	0.218	0.225	0.345				284	293	449	-	-	-
L1-4	4	21,587	1,240	0.206	0.202	0.231	0.332			255	250	286	411	-	-
L1-5	5	20,403	1,184	0.191	0.182	0.190	0.207	0.284	0.306	226	216	225	244	336	362
L1-6	6	19,269	1,133	0.192	0.182	0.181	0.185	0.201	0.206	218	206	205	210	228	234
L1-7	7	18,181	1,088	0.174	0.163	0.160	0.159	0.162	0.164	190	178	174	173	176	179
L1-8	8	17,132	1,049	0.175	0.163	0.157	0.154	0.154	0.151	183	171	165	162	161	159
L1-9	9	16,115	1,016	0.158	0.146	0.140	0.136	0.134	0.132	161	149	143	139	136	134
L1-10	10	15,126	989	0.165	0.153	0.145	0.141	0.137	0.134	163	151	144	139	136	132
L1-11	11	14,159	968	0.159	0.147	0.139	0.134	0.130	0.126	154	142	135	130	125	122
L1-12	12	13,207	952	0.140	0.129	0.122	0.117	0.112	0.110	133	123	116	111	107	104
L1-13	13	12,265	942	0.142	0.131	0.123	0.118	0.113	0.109	134	123	116	111	107	103
L1-14	14	11,327	938	0.115	0.106	0.099	0.095	0.091	0.089	108	99	93	89	85	83
L1-15	15	10,387	940	0.099	0.091	0.085	0.082	0.078	0.076	93	86	80	77	73	71
L1-16	16	9,440	947	0.087	0.081	0.075	0.072	0.069	0.067	83	76	71	68	65	63
L1-17	17	8,479	961	0.082	0.076	0.071	0.068	0.065	0.063	79	73	68	65	62	60
L1-18	18	7,499	980	0.076	0.071	0.066	0.063	0.060	0.058	75	69	65	62	59	57
L1-19	19	6,494	1,005	0.079	0.073	0.068	0.066	0.063	0.060	80	74	69	66	63	61
L1-20	20	5,458	1,036	0.074	0.069	0.064	0.061	0.058	0.056	77	71	66	63	60	59
L1-21	21	4,385	1,073	0.114	0.106	0.099	0.094	0.089	0.087	123	114	106	101	96	94
L1-22	22	3,270	1,115	0.070	0.065	0.061	0.060	0.057	0.054	78	73	68	67	63	60
L1-23	23	2,106	1,164	0.034	0.033	0.031	0.030	0.028	0.027	40	38	36	35	33	31
L1-24	24	888	2,106	0.066	0.062	0.059	0.059	0.055	0.053	138	132	123	123	116	111

Appendix 2. L2 output for velocity and volumetric flow rate with K dataset 4

Height Interval	Depth From top (cm)	SA-3D (cm ²)	SA-Change (cm ²)	Velocity (T=275) (cm/min)	Velocity (T=280) (cm/min)	Velocity (T=285) (cm/min)	Velocity (T=290) (cm/min)	Velocity (T=295) (cm/min)	Velocity (T=300) (cm/min)	Q int (T=275) (cm ³ /min)	Q int (T=280) (cm ³ /min)	Q int (T=285) (cm ³ /min)	Q int (T=290) (cm ³ /min)	Q int (T=295) (cm ³ /min)	Q int (T=300) (cm ³ /min)
L2-0	0	39,828	-							-	-	-	-	-	-
L2-1	1	37,254	2,574	0.136						350	-	-	-	-	-
L2-2	2	34,987	2,267	0.053	0.184					120	417	-	-	-	-
L2-3	3	32,987	1,999	0.052	0.089					104	177	-	-	-	-
L2-4	4	31,219	1,768	0.040	0.050	0.104				70	88	183	-	-	-
L2-5	5	29,647	1,572	0.095	0.100	0.115	0.200			149	157	181	314	-	-
L2-6	6	28,240	1,407	0.056	0.059	0.066	0.107	0.147		79	83	93	151	206	-
L2-7	7	26,968	1,272	0.072	0.073	0.078	0.098	0.158		92	93	99	124	201	-
L2-8	8	25,804	1,164	0.083	0.086	0.093	0.118	0.152	0.240	97	100	108	138	177	280
L2-9	9	24,723	1,081	0.102	0.103	0.107	0.122	0.139	0.160	111	111	116	132	150	173
L2-10	10	23,702	1,021	0.084	0.087	0.094	0.112	0.122	0.133	86	89	96	115	125	136
L2-11	11	22,720	981	0.085	0.087	0.095	0.110	0.117	0.123	83	86	93	108	115	121
L2-12	12	21,761	959	0.099	0.099	0.103	0.112	0.116	0.118	95	95	98	107	111	114
L2-13	13	20,808	953	0.084	0.087	0.094	0.106	0.109	0.111	80	83	89	101	104	106
L2-14	14	19,849	959	0.093	0.093	0.097	0.103	0.105	0.105	90	90	93	99	101	101
L2-15	15	18,872	977	0.078	0.081	0.087	0.096	0.099	0.099	76	79	85	94	96	97
L2-16	16	17,870	1,002	0.086	0.086	0.089	0.093	0.094	0.094	86	86	89	94	94	94
L2-17	17	16,836	1,034	0.077	0.079	0.085	0.092	0.093	0.093	79	82	88	95	96	96
L2-18	18	15,767	1,069	0.076	0.078	0.083	0.089	0.090	0.089	82	84	89	95	96	95
L2-19	19	14,661	1,106	0.080	0.080	0.081	0.084	0.084	0.082	88	88	90	93	93	91
L2-20	20	13,519	1,142	0.072	0.074	0.077	0.081	0.081	0.080	82	84	88	92	93	91
L2-21	21	12,345	1,174	0.070	0.069	0.070	0.071	0.070	0.069	82	81	82	83	82	81
L2-22	22	11,145	1,200	0.057	0.057	0.058	0.059	0.059	0.058	68	68	70	71	71	69
L2-23	23	9,926	1,219	0.051	0.051	0.052	0.053	0.052	0.051	62	62	63	64	64	62
L2-24	24	8,699	1,227	0.049	0.049	0.049	0.050	0.050	0.049	60	60	61	62	61	60
L2-25	25	7,478	1,222	0.05119	0.04986	0.04966	0.04952	0.04852	0.04728	63	61	61	60	59	58
L2-26	26	6,277	1,201	0.04596	0.04599	0.04702	0.04788	0.047485	0.04647	55	55	56	58	57	56
L2-27	27	5,113	1,163	0.052	0.05036	0.04994	0.04939	0.048197	0.04693	60	59	58	57	56	55
L2-28	28	4,008	1,105	0.08392	0.08059	0.07933	0.07784	0.075607	0.0733	93	89	88	86	84	81
L2-29	29	2,983	1,025	0.0457	0.04513	0.04554	0.04572	0.045105	0.04445	47	46	47	47	46	46
L2-30	30	2,062	2,983	0.02946	0.02814	0.02758	0.02679	0.025907	0.02562	88	84	82	80	77	76

Appendix 3. L3 output for velocity and volumetric flow rate with K dataset 4

Site	Depth From top (cm)	SA-3D (cm ²)	SA-Change (cm ²)	Velocity (T=235) (cm/min)	Velocity (T=240) (cm/min)	Velocity (T=245) (cm/min)	Velocity (T=250) (cm/min)	Velocity (T=255) (cm/min)	Velocity (T=260) (cm/min)	Q int (T=235) (cm ³ /min)	Q int (T=240) (cm ³ /min)	Q int (T=245) (cm ³ /min)	Q int (T=250) (cm ³ /min)	Q int (T=255) (cm ³ /min)	Q int (T=260) (cm ³ /min)
L3-0	0	20,867	1,487							-	-	-	-	-	-
L3-1	1	19,380	1,472	0.38638						569	-	-	-	-	-
L3-2	2	17,908	1,448	0.23766	0.326					344	471	-	-	-	-
L3-3	3	16,460	1,416	0.21348	0.336	0.298				302	475	421	-	-	-
L3-4	4	15,045	1,377	0.19127	0.211	0.261	0.347			263	290	360	477	-	-
L3-5	5	13,668	1,331	0.16358	0.163	0.164	0.192	0.283	0.305	218	217	219	256	377	406
L3-6	6	12,337	1,281	0.1611	0.156	0.154	0.163	0.183	0.188	206	200	198	209	234	240
L3-7	7	11,055	1,227	0.13091	0.124	0.120	0.123	0.126	0.128	161	152	147	150	154	157
L3-8	8	9,828	1,170	0.1109	0.104	0.099	0.099	0.098	0.097	130	122	116	116	115	113
L3-9	9	8,658	1,112	0.09732	0.090	0.086	0.084	0.082	0.080	108	100	95	94	91	89
L3-10	10	7,546	1,052	0.09093	0.084	0.079	0.077	0.075	0.072	96	88	83	81	78	76
L3-11	11	6,494	992	0.08532	0.078	0.074	0.072	0.069	0.067	85	78	74	72	69	66
L3-12	12	5,502	934	0.08649	0.080	0.075	0.073	0.069	0.066	81	74	70	68	64	61
L3-13	13	4,568	878	0.08197	0.075	0.071	0.069	0.065	0.062	72	66	62	60	57	55
L3-14	14	3,690	824	0.12874	0.117	0.110	0.106	0.101	0.097	106	97	91	87	83	80
L3-15	15	2,866	776	0.07314	0.068	0.064	0.064	0.060	0.056	57	53	50	49	46	44
L3-16	16	2,090	2,090	0.03438	0.033	0.032	0.032	0.030	0.028	72	69	66	67	63	59

Appendix 4. L4 output for velocity and volumetric flow rate with K dataset 4

Site	Depth From top (cm)	SA-3D (cm ²)	SA-Change (cm ²)	Velocity (T=275) (cm/min)	Velocity (T=280) (cm/min)	Velocity (T=285) (cm/min)	Velocity (T=290) (cm/min)	Velocity (T=295) (cm/min)	Velocity (T=300) (cm/min)	Q int (T=275) (cm ³ /min)	Q int (T=280) (cm ³ /min)	Q int (T=285) (cm ³ /min)	Q int (T=290) (cm ³ /min)	Q int (T=295) (cm ³ /min)	Q int (T=300) (cm ³ /min)
L4-0	0	31,038	-							-	-	-	-	-	-
L4-1	1	29,256	1,782	0.263						469	-	-	-	-	-
L4-2	2	27,685	1,571	0.196	0.378					307	594	-	-	-	-
L4-3	3	26,289	1,396	0.207	0.280					289	391	-	-	-	-
L4-4	4	25,037	1,253	0.200	0.219	0.335				251	274	420	-	-	-
L4-5	5	23,897	1,140	0.201	0.201	0.229	0.356			230	229	261	406	-	-
L4-6	6	22,843	1,054	0.195	0.188	0.194	0.242			206	198	204	256	-	-
L4-7	7	21,851	993	0.200	0.188	0.185	0.192	0.314		199	187	184	191	311	-
L4-8	8	20,898	953	0.186	0.173	0.167	0.167	0.192	0.300	178	165	159	159	183	286
L4-9	9	19,965	933	0.189	0.173	0.164	0.158	0.166	0.196	176	161	153	148	155	183
L4-10	10	19,036	929	0.174	0.158	0.149	0.143	0.143	0.154	162	147	138	133	133	143
L4-11	11	18,097	939	0.184	0.165	0.154	0.146	0.143	0.145	173	155	145	137	134	136
L4-12	12	17,137	960	0.167	0.150	0.139	0.131	0.127	0.127	160	144	134	126	122	122
L4-13	13	16,148	989	0.191	0.169	0.155	0.144	0.137	0.133	189	167	153	142	136	132
L4-14	14	15,125	1,024	0.153	0.136	0.126	0.117	0.111	0.108	156	139	129	120	113	111
L4-15	15	14,064	1,061	0.144	0.127	0.116	0.108	0.101	0.098	153	135	123	114	108	104
L4-16	16	12,964	1,099	0.116	0.103	0.095	0.088	0.083	0.080	128	113	105	97	91	88
L4-17	17	11,830	1,135	0.108	0.095	0.087	0.080	0.075	0.072	123	108	99	91	85	82
L4-18	18	10,665	1,165	0.099	0.087	0.080	0.074	0.069	0.066	116	102	93	86	80	76
L4-19	19	9,478	1,187	0.096	0.085	0.078	0.071	0.066	0.063	114	100	92	85	79	75
L4-20	20	8,280	1,199	0.089	0.079	0.073	0.067	0.062	0.060	107	95	87	80	75	72
L4-21	21	7,083	1,197	0.095	0.083	0.076	0.070	0.065	0.061	113	99	91	84	77	73
L4-22	22	5,904	1,179	0.154	0.137	0.125	0.114	0.107	0.104	182	162	148	135	126	123
L4-23	23	4,761	1,143	0.084	0.075	0.071	0.066	0.060	0.057	96	86	81	75	69	65
L4-24	24	3,676	1,085	0.040	0.037	0.037	0.034	0.032	0.030	43	40	40	37	34	32
L4-25	25	2,673	1,003	0.044	0.041	0.040	0.038	0.035	0.033	44	41	41	38	35	33
L4-26	26	1,779	894	0.076	0.072	0.074	0.070	0.064	0.060	68	64	66	62	57	54
L4-27	27	1,023	756	0.076	0.072	0.074	0.070	0.064	0.060	57	54	56	53	48	45
L4-28	28	438	585	0.076	0.072	0.074	0.070	0.064	0.060	44	42	43	41	37	35

Appendix 5. U1 output for velocity and volumetric flow rate with K dataset 4

Site	Depth From top (cm)	SA-3D (cm ²)	SA-Change (cm ²)	Velocity (T=240) (cm/min)	Velocity (T=245) (cm/min)	Velocity (T=250) (cm/min)	Velocity (T=255) (cm/min)	Velocity (T=260) (cm/min)	Velocity (T=265) (cm/min)	Q int (T=240) (cm ³ /min)	Q int (T=245) (cm ³ /min)	Q int (T=250) (cm ³ /min)	Q int (T=255) (cm ³ /min)	Q int (T=260) (cm ³ /min)	Q int (T=265) (cm ³ /min)
U1-0	0	24,834	-							-	-	-	-	-	-
U1-1	1	23,614	1,219	0.861						1,050	-	-	-	-	-
U1-2	2	22,448	1,166	0.428	0.648					499	755	-	-	-	-
U1-3	3	21,324	1,124	0.394	0.431	0.748				443	485	841	-	-	-
U1-4	4	20,232	1,092	0.307	0.309	0.369	0.575	0.485		335	338	403	628	530	-
U1-5	5	19,163	1,068	0.322	0.314	0.329	0.370	0.582		344	336	351	395	622	-
U1-6	6	18,112	1,052	0.268	0.256	0.257	0.267	0.296	0.520	281	269	271	280	311	547
U1-7	7	17,071	1,041	0.283	0.267	0.261	0.263	0.276	0.329	294	278	272	273	287	342
U1-8	8	16,035	1,035	0.205	0.193	0.186	0.182	0.183	0.197	213	199	192	188	189	204
U1-9	9	15,002	1,034	0.179	0.166	0.158	0.153	0.151	0.155	185	172	163	158	156	160
U1-10	10	13,968	1,034	0.174	0.161	0.151	0.145	0.141	0.141	180	167	156	150	145	145
U1-11	11	12,932	1,036	0.155	0.144	0.135	0.129	0.125	0.124	161	149	140	133	129	128
U1-12	12	11,894	1,038	0.147	0.135	0.126	0.119	0.114	0.112	152	140	130	124	119	116
U1-13	13	10,856	1,038	0.122	0.112	0.104	0.098	0.094	0.092	126	116	108	102	97	95
U1-14	14	9,819	1,037	0.106	0.097	0.089	0.084	0.080	0.078	110	100	93	87	83	81
U1-15	15	8,787	1,032	0.095	0.086	0.079	0.075	0.071	0.068	98	89	82	77	73	71
U1-16	16	7,765	1,022	0.083	0.076	0.069	0.065	0.062	0.060	85	78	71	67	63	61
U1-17	17	6,759	1,006	0.066	0.061	0.055	0.052	0.049	0.047	67	61	56	52	50	48
U1-18	18	5,776	983	0.053	0.048	0.044	0.042	0.039	0.038	52	48	44	41	39	37
U1-19	19	4,825	951	0.046	0.042	0.039	0.037	0.035	0.034	44	40	37	35	33	32
U1-20	20	3,914	910	0.052	0.049	0.046	0.045	0.043	0.042	47	44	42	41	39	38
U1-21	21	3,056	859	0.056	0.054	0.051	0.050	0.048	0.047	48	46	44	43	42	40
U1-22	22	2,261	795	0.063	0.061	0.058	0.057	0.055	0.053	50	48	46	45	44	42
U1-23	23	1,543	718	0.076	0.074	0.072	0.071	0.070	0.067	55	53	52	51	50	48
U1-24	24	916	916	0.071	0.069	0.067	0.066	0.066	0.063	65	63	62	61	60	58

Appendix 6. U3 output for velocity and volumetric flow rate with K dataset 4

Site	Depth From top (cm)	SA-3D (cm ²)	SA-Change (cm ²)	Velocity (T=250) (cm/min)	Velocity (T=255) (cm/min)	Velocity (T=260) (cm/min)	Velocity (T=265) (cm/min)	Velocity (T=270) (cm/min)	Velocity (T=275) (cm/min)	Q int (T=250) (cm ³ /min)	Q int (T=255) (cm ³ /min)	Q int (T=260) (cm ³ /min)	Q int (T=265) (cm ³ /min)	Q int (T=270) (cm ³ /min)	Q int (T=275) (cm ³ /min)
U3-0	0	30,076		0.75673						-	-	-	-	-	-
U3-1	1	28,768	1,309	0.39767						520	-	-	-	-	-
U3-2	2	27,557	1,210	0.36083	0.70583					437	854	-	-	-	-
U3-3	3	26,428	1,130	0.33222	0.40461					375	457	-	-	-	-
U3-4	4	25,363	1,065	0.27927	0.29613	0.6345				297	315	676	-	-	-
U3-5	5	24,349	1,014	0.29674	0.29181	0.36926				301	296	375	-	-	-
U3-6	6	23,371	977	0.24801	0.23776	0.25947	0.57582			242	232	254	563	-	-
U3-7	7	22,419	952	0.26936	0.25093	0.25239	0.32794			256	239	240	312	-	-
U3-8	8	21,482	938	0.22901	0.21204	0.20737	0.23358	0.432203		215	199	194	219	405	-
U3-9	9	20,549	933	0.24416	0.22287	0.21242	0.22001	0.27034		228	208	198	205	252	-
U3-10	10	19,613	936	0.17982	0.16435	0.15537	0.15626	0.166767	0.33351	168	154	145	146	156	312
U3-11	11	18,668	945	0.15724	0.14246	0.13278	0.1294	0.130925	0.15902	149	135	126	122	124	150
U3-12	12	17,708	960	0.15377	0.13804	0.12697	0.12072	0.117987	0.12743	148	133	122	116	113	122
U3-13	13	16,728	980	0.13717	0.12431	0.11519	0.11043	0.107187	0.11193	134	122	113	108	105	110
U3-14	14	15,726	1,002	0.12973	0.11658	0.10686	0.10057	0.095816	0.09565	130	117	107	101	96	96
U3-15	15	14,701	1,025	0.10727	0.09669	0.08879	0.08358	0.079312	0.07815	110	99	91	86	81	80
U3-16	16	13,652	1,049	0.09286	0.08358	0.07652	0.07159	0.067452	0.06545	97	88	80	75	71	69
U3-17	17	12,581	1,071	0.08286	0.0746	0.06824	0.06365	0.059724	0.05747	89	80	73	68	64	62
U3-18	18	11,489	1,091	0.07277	0.06559	0.05999	0.05586	0.052281	0.05003	79	72	65	61	57	55
U3-19	19	10,382	1,108	0.05843	0.05273	0.04822	0.04475	0.041709	0.03963	65	58	53	50	46	44
U3-20	20	9,263	1,119	0.04683	0.04276	0.03948	0.03683	0.034296	0.03245	52	48	44	41	38	36
U3-21	21	8,139	1,124	0.04139	0.03824	0.03562	0.03336	0.031066	0.02932	47	43	40	37	35	33
U3-22	22	7,018	1,121	0.05032	0.04743	0.04484	0.04218	0.039312	0.03707	56	53	50	47	44	42
U3-23	23	5,909	1,109	0.05602	0.05306	0.05033	0.0474	0.044178	0.04161	62	59	56	53	49	46
U3-24	24	4,823	1,087	0.06378	0.0605	0.05727	0.05395	0.05035	0.04742	69	66	62	59	55	52
U3-25	25	3,770	1,053	0.07979	0.07658	0.07191	0.06774	0.063447	0.05985	84	81	76	71	67	63
U3-26	26	2,764	1,006	0.07475	0.07159	0.06717	0.06309	0.058939	0.05555	75	72	68	63	59	56
U3-27	27	1,819	945	0.07475	0.07159	0.06717	0.06309	0.058939	0.05555	71	68	63	60	56	52
U3-28	28	951	868	0.07475	0.07159	0.06717	0.06309	0.058939	0.05555	65	62	58	55	51	48
U3-29	29	177	774	0.07475	0.07159	0.06717	0.06309	0.058939	0.05555	58	55	52	49	46	43

Appendix 7. U4 output for velocity and volumetric flow rate with K dataset 4

Site	Depth From top (cm)	SA-3D (cm2)	SA-Change (cm2)	Velocity (T=250) (cm/min)	Velocity (T=255) (cm/min)	Velocity (T=260) (cm/min)	Velocity (T=265) (cm/min)	Velocity (T=270) (cm/min)	Velocity (T=275) (cm/min)	Q int (T=250) (cm ³ /min)	Q int (T=255) (cm ³ /min)	Q int (T=260) (cm ³ /min)	Q int (T=265) (cm ³ /min)	Q int (T=270) (cm ³ /min)	Q int (T=275) (cm ³ /min)
U4-0	0	50,299	-	0.36812						-	-	-	-	-	-
U4-1	1	46,968	3,332	0.17414						580	-	-	-	-	-
U4-2	2	43,966	3,002	0.14174	0.43482					425	1,305	-	-	-	-
U4-3	3	41,263	2,703	0.16602	0.21623					449	585	-	-	-	-
U4-4	4	38,828	2,435	0.16847	0.19691	0.40948				410	479	997	-	-	-
U4-5	5	36,632	2,195	0.14156	0.15864	0.18966	0.32009			311	348	416	703	-	-
U4-6	6	34,649	1,983	0.13087	0.1386	0.14675	0.17109			259	275	291	339	-	-
U4-7	7	32,854	1,796	0.13579	0.1598	0.1685	0.17744	0.387587		244	287	303	319	696	-
U4-8	8	31,221	1,633	0.1901	0.19947	0.20046	0.20556	0.270577	0.53678	310	326	327	336	442	876
U4-9	9	29,728	1,492	0.19049	0.21074	0.21144	0.20946	0.241465	0.31016	284	314	316	313	360	463
U4-10	10	28,355	1,373	0.19484	0.21276	0.21104	0.2065	0.225165	0.253	268	292	290	284	309	347
U4-11	11	27,082	1,273	0.1951	0.19954	0.19334	0.18738	0.194567	0.20427	248	254	246	239	248	260
U4-12	12	25,891	1,191	0.19863	0.21159	0.20597	0.19747	0.20129	0.2033	237	252	245	235	240	242
U4-13	13	24,765	1,126	0.18657	0.18872	0.18064	0.17218	0.171497	0.16994	210	213	203	194	193	191
U4-14	14	23,689	1,076	0.19268	0.20163	0.19408	0.18392	0.181745	0.1773	207	217	209	198	196	191
U4-15	15	22,650	1,039	0.18131	0.18076	0.17144	0.16176	0.157543	0.15248	188	188	178	168	164	158
U4-16	16	21,636	1,014	0.18527	0.18921	0.18035	0.16965	0.16467	0.15819	188	192	183	172	167	160
U4-17	17	20,635	1,000	0.15333	0.14817	0.13889	0.13005	0.124673	0.11928	153	148	139	130	125	119
U4-18	18	19,641	995	0.13187	0.12857	0.12073	0.11277	0.107745	0.10258	131	128	120	112	107	102
U4-19	19	18,644	997	0.12539	0.12373	0.11662	0.10879	0.103694	0.09827	125	123	116	108	103	98
U4-20	20	17,638	1,005	0.12528	0.11782	0.10929	0.10148	0.096047	0.09109	126	118	110	102	97	92
U4-21	21	16,621	1,018	0.11407	0.109	0.10166	0.09437	0.089276	0.08439	116	111	103	96	91	86
U4-22	22	15,587	1,033	0.09847	0.09272	0.08597	0.07955	0.07502	0.07089	102	96	89	82	78	73
U4-23	23	14,537	1,051	0.08553	0.08062	0.07475	0.06909	0.065084	0.06143	90	85	79	73	68	65
U4-24	24	13,469	1,067	0.07708	0.07259	0.06727	0.06213	0.058478	0.05517	82	77	72	66	62	59
U4-25	25	12,386	1,083	0.06836	0.06438	0.05965	0.05509	0.051826	0.04889	74	70	65	60	56	53
U4-26	26	11,291	1,095	0.05516	0.05207	0.04837	0.0448	0.042207	0.03986	60	57	53	49	46	44
U4-27	27	10,188	1,103	0.04761	0.04464	0.04138	0.03843	0.036231	0.03434	53	49	46	42	40	38
U4-28	28	9,083	1,105	0.04374	0.04113	0.03815	0.03556	0.033614	0.03197	48	45	42	39	37	35
U4-29	29	7,984	1,099	0.05503	0.05193	0.04833	0.04542	0.043185	0.04133	60	57	53	50	47	45
U4-30	30	6,901	1,084	0.06185	0.05852	0.0544	0.05122	0.048757	0.04672	67	63	59	56	53	51
U4-31	31	5,843	1,058	0.07044	0.06677	0.06183	0.05813	0.055294	0.05296	75	71	65	62	59	56
U4-32	32	4,822	1,020	0.08798	0.08343	0.07738	0.07279	0.069311	0.06651	90	85	79	74	71	68
U4-33	33	3,853	969	0.08216	0.07732	0.07177	0.0675	0.064218	0.06156	80	75	70	65	62	60
U4-34	34	2,951	902	0.08216	0.07732	0.07177	0.0675	0.064218	0.06156	74	70	65	61	58	56